UNIVERSITY OF OSLO
Department of Geosciences - Meteorology and Oceanography section.

A study on atmospheric relative dispersion using the transport model FLEXPART

Master thesis in Geosciences Meteorology and Oceanography

Sigmund Guttu

1st June 2011

Abstract

Relative dispersion is a widely used measure to characterize mixing properties of atmospheric passive tracers. Numerical models allow for a large number of particles. In this thesis, the Lagrangian transport model FLEXPART has been used to generate particle trajectories. The advection velocity field was provided by the European Centre for Medium-Range Weather Forecasts (ECMWF). 40000 particles were deployed along latitude lines, at 30N and 30S, 60N and 60S, and at two heights, (6km and 12km). Trajectories on all these locations were made in two different months, January and September 2009. The initial particle separation was determined by the grid spacing for the winds,$1^o \times 1^o$.

In addition to relative dispersion, we examine probability density functions (PDFs) of pair separations. To interpret the results, we also consider the second order (Eulerian) structure functions. Up to a few hundred kilometers, an exponential dispersion regime was detected by the relative dispersion, while the separation distributions (PDFs) indicated that the nonlocal dispersion is likely to extend to the deformation radius. The structure functions are consistent with exponential growth, and suggest the large scale behavior is probably diffusive.

Acknowledgement

I would like to thank my supervisor Joseph Henry LaCasce for an inspiring and encouraging guidance throughout the work with this thesis. His knowledge on the topic has been of high importance for my understandings of the results. Sabine Eckhardt and Nina Iren Kristiansen at NILU also deserve great credits for helping me with some issues regarding the numerical model FLEXPART. It was crucial for me in having progress at an early stage of my work.

Also great thanks to my fellow students, including the hard working Bergen girl at my right hand side, with whom I have developed a friendship throughout the five years as a student in Oslo, the Vålerenga supporter opposite to me providing restful moments with unserious football discussions and the funny Spanish guy in the right corner of the study hall.

I will of course thank Karianne for being patient and encouraging me, especially in the very end of this long period. Also father, mother and brother deserve great credits for raising me as the person I am and always supporting my choices throughout my life.

Contents

Chapter 1

Introduction

The air that continuously moves around in the Earth's atmosphere forms a complex physical system which has challenged scientists for thousands of years. Some of its complexity is illustrated by Figure 1.1, which shows a simulated ensemble of fluid particles drifting around 6km above the European continent. The abrupt changes in the particle motion provide a fairly chaotic view of the flow field, an indication of turbulence. Highly irregular motion like this is only described statistically. Although progress has been made, continued lack of knowledge makes this topic a prioritized field in atmospheric research environments. The actuality of some of the issues that atmospheric turbulence cover, does also reflect a discipline of high practical relevance.

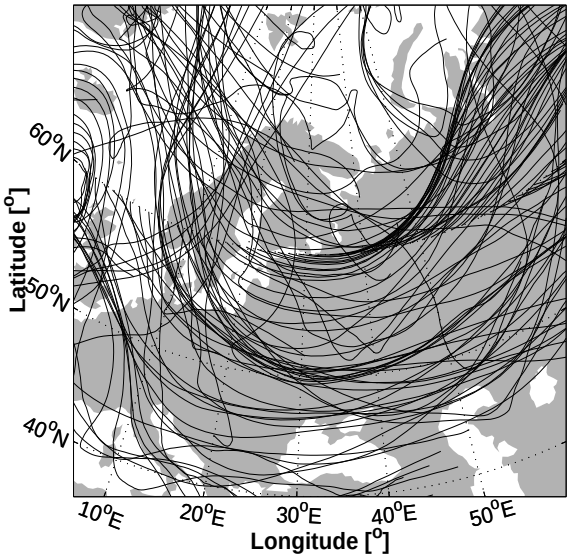

Figure 1.1: Trajectories of air parcels over Europe deployed at 60^o North in January 2009. Generated by the Lagrangian transport model Flexpart

Atmospheric motion consists of a wide range of spatial and temporal scales, shown in Figure 1.2, associated by different phenomena, from the very small viscous processes dissipating kinetic energy to the large

planetary waves feeding energy to the high and low pressure systems. In between these two extremes, i.e. at intermediate scales, wave interactions cause a continuous transfer of energy among different scales of motion. These interactions cause major mixing and transport of atmospheric components, e.g. chemical species, contaminants, etc., and is crucial to how these are spread and distributed.

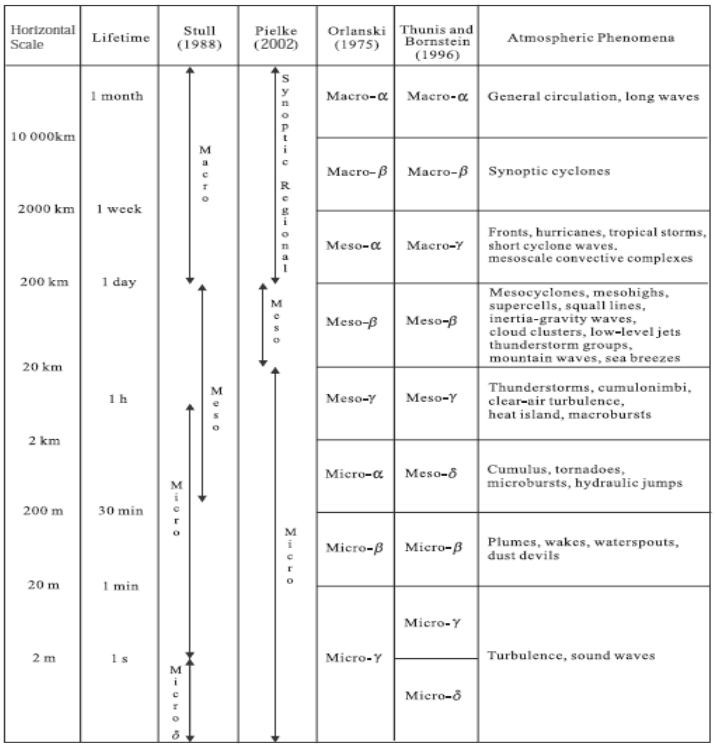

Figure 1.2: Atmospheric scale definitions. From Lin (2007)

Recent accidents have showed the importance of predicting where pollutants are transported. After the Eyjafjallajökull eruption in spring 2010, the European aviation authorities were heavily dependent on reliable information about where the ash clouds were advected. Another eruption at Grimsvötn volcano in May 2011 has actualized the topic. The recent nuclear eruption in Japan also showed the importance of an operative system, which predicts in which direction the hazardous substances are spreading. In a future disaster, an improvement of the predictions could be crucial for a large number of humans and animals. Another current issue concerns climate and how it possibly changes due to an increase in the amount of atmospheric greenhouse gases. The distribution and seasonal cycles of those is important to be well understood in a scientific problem of such a complexity.

To acquire knowledge on how pollutants and other components, often called passive tracers, are drifting around in the atmosphere, one approach is to send up balloons and track their paths. A method used to measure

the balloon dispersion is to calculate their mean displacement relative to the starting position, i.e. absolute dispersion. However, a more proper method to describe how a tracer cloud is spreading is to consider balloon pairs. The variance of the pair separations yields a measure called relative dispersion. This measure reflects different types of flow, which is essential to ensure a realistic description of tracer spreading. Hence, this is a widely used method to characterize transport and mixing properties of atmospheric tracers.

The topic covering atmospheric dispersion has been paid increasingly attention to during the last century. Richardson (1926) studied smoke from factory stacks and detected a striking relation between the particle diffusivity and separation between the particles. That is

$$K \propto r^{4/3} \tag{1.1}$$

where

$$K(t) \equiv \frac{1}{2}\frac{d}{dt}\overline{r^2}$$

is the relative diffusivity and r is the separations between the particles.

The relation in (1.1) is known as Richardson's law and states that the growth of a tracer cloud is dependent on the size of the cloud. This detection was a milestone at that time. However, an extension of observational research like this has been difficult to achieve. Balloon projects were both expensive and challenging. In the decades after Richardson's work, most progress was made on establishing a theoretical framework for atmospheric turbulence. Since the turbulent flow directly affects the dispersion of tracers, the development of a robust theory for turbulence has been of high importance.

The kinetic energy spectrum was inferred to be a useful tool to characterize the turbulent flow. Kolmogorov (1941) considered a range of scales in between the scales at which forcing and dissipation are affecting the flow. The turbulence was assumed to be isotropic, homogenous and stationary in this range, known as the inertial range. Under these conditions, he predicted a kinetic energy spectrum proportional to scale.

$$E(k) \propto \epsilon^{2/3} k^{-5/3} \tag{1.2}$$

where ϵ is the energy flux and k is the wavenumber. Figure 1.3 shows the Kolmogorov energy spectrum.

This spectrum was deduced for a three dimensional (3-D) turbulent fluid. When the vertical component of the velocity field is much smaller than the horizontal components, the motion is thought to be approximately two dimensional (2-D). Kraichnan (1967) suggested two inertial ranges using the same arguments as Kolmogorov. One, characterized by an upscale transfer

of energy, provided the same kinetic energy spectrum as (1.2). The additional range was based on a transfer of another inviscid quantity, enstrophy, downscale. Enstrophy is defined as the vorticity squared. A turbulent flow dominated by an enstrophy transfer was associated by a kinetic energy spectrum expressed as

$$E(k) \propto \eta^{2/3} k^{-3} \tag{1.3}$$

where η is the enstrophy flux.

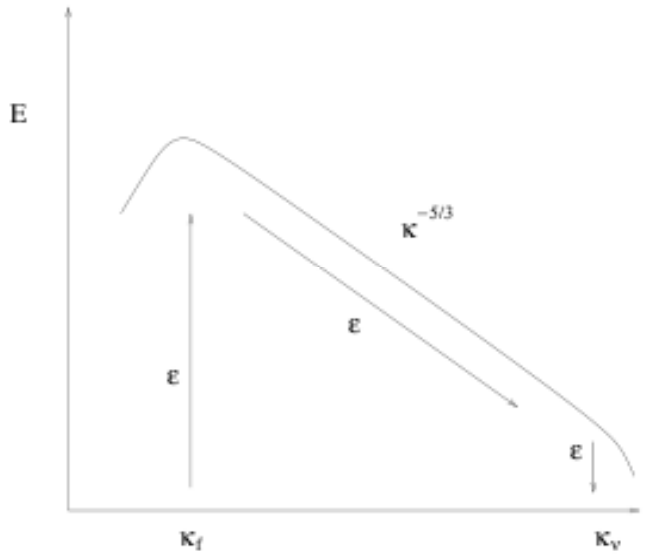

Figure 1.3: The Kolmogorov energy spectrum. The y axis displays the energy per wavenumber $E(\kappa)$ while the x axis displays the scale in wavenumber κ. κ_f denotes the scale of energy input, i.e. forcing, and κ_ν is the scale of energy dissipation, i.e. damping. From LaCasce (2011)

In the free atmosphere, above the highly 3-D atmospheric boundary layer and far from areas dominated by strong convective motions, the quasi-geostrophic (QG) approximation is a reasonable description of the flow field. Charney (1971) showed that 2-D turbulence theory applied to describe the turbulent processes associated with QG motion. The relative dispersion at these scales is then determined by the predicted spectrum in (1.2) and (1.3). While Richardson's law yields a cubic growth of the particle separation in a $k^{-5/3}$ energy spectrum, Lin (1972) suggested that particle separations are growing exponentially in time in a k^{-3} spectrum.

In the 70's, new satellite technology allowed scientists to track balloon paths. Two balloon experiments, EOLE and TWERLE (Tropospheric Wind Earth Radio Location Experiment), performed in the Southern hemisphere, were examined by Morel and Larcheveque (1974) and Er-El and Peskin (1981) to study the turbulent dispersion. The balloons were deployed at

200hPa and 150hPa, respectively. Both suggested relative dispersion obeying Lin's exponential law up to separations of 1000km. Lacorata et al. (2004) and LaCasce (2010) reexamined the EOLE data using additional measures to detect the mesoscale dispersion. While the former study suggested Richardson growth, the latter suggested exponential growth, at least up to a few hundred kilometers. Together with other contradicting results, this ensures a topic which is continuously under debate. Calculations of kinetic energy spectra could alternatively broaden the debate. Desbois (1975) used the wind data from the EOLE experiment to infer a spectrum with a shape close to k^{-3}, in line with Morel and Larcheveque (1974). The GASP (Global Atmospheric Sampling Program) program provided a large set of wind data, collected from over 6900 flights of commercial aircrafts. Nastrom and Gage (1984) calculated the Eulerian kinetic energy spectrum, which indicated a k^{-3} spectrum from wavelengths from a few hundred kilometers up to about three thousands kilometers. The smallest scale showed a $k^{-5/3}$ dependence.

The debate on how turbulence behaves at the atmospheric mesoscale concerns a lot of issues in the meteorological discipline today. The numerical models which provide weather predictions are important for a variety of purposes, e.g. forecasting extreme weather. These are restricted in space and time resolution due to limited computing power. Therefore, a satisfactory parameterization of the flow field below the grid scale is important to improve the model's reliability (Basdevant et al., 1978). A simple and realistic description of the energy transfer, i.e. an energy spectrum, is crucial to ensure this. Since relative dispersion concerns separation growth in time, it also predicts the evolution of small position errors made in the initializations of a weather forecast. Whether this growth is exponential and heavily dependent on the initial error (Lorenz, 1969) or not, e.g. obeying Richardson's law, would eventually affect the budget priorities of the authorities. It is not worth spending money on more accurate measurements if the forecast error is independent of the initial condition.

In this thesis, the goal is to improve the understanding of turbulent relative dispersion in the atmosphere in light of earlier studies. Since the theory of turbulence restricts to a statistical description, a huge number of particles are required to ensure stable statistics. The EOLE and TWERLE projects provided remarkable results, but the data are somewhat noisy, especially when the balloons have spread to a wide range of scales. The use of numerical transport models, however, allows us to use a huge number of particles, which will act as balloons. In addition, this is almost costless. In this study, the Lagrangian transport model FLEXPART with reanalysis wind field from the European Centre for Medium-Range Weather Forecasts (ECMWF) has been used to generate trajectories of so-called "synthetic balloons". Motivated by the climatological study of Huber et al. (2001), two heights, 6km and 12km, at two latitudes, 60^o and 30^o, in each hemisphere have been tested to check if relative dispersion is universal. Initially, 40000 particles are displaced uniformly around a latitude circle. Two months, January and September 2009, were used to detect possible seasonal vari-

ations. The simulations lasted for one month. An extended description of FLEXPART is given in Chapter 2.

In Chapter 3, the theoretical framework for this study is presented. The basics of two dimensional turbulence are shortly described and are followed by an introduction to turbulent dispersion. This covers absolute dispersion, relative dispersion and its relation to the underlying turbulent flow, described by the Eulerian kinetic energy spectrum. However, relative dispersion as a measure tends to fail under influence of large scales, where dispersion does not satisfy the basic assumptions of 2-D turbulence. The separation distribution, of which relative dispersion is the variance, is a more conclusive tool. Thus, some probability density functions (PDF) reflecting the different turbulent flow predictions are presented in the last section. A subsequent short chapter extends the presentation of earlier studies with a more detailed description of their results.

The results of the data obtained by FLEXPART are presented in Chapter 5. First, the data's consistency upon the theoretical assumptions are tested. Then the physical results are presented, i.e figures showing relative dispersion and PDFs. Finally, the Eulerian kinetic energy spectrum and its related second-order structure functions based on the input wind velocity data from ECMWF, are shown to extend the discussion in light of the relation to relative dispersion. The subsequent Chapter 6 contains a discussion of the results. The most important results are summarized, and some concluding remarks are pointed out in Chapter 7.

Chapter 2

Method

In this chapter, the method for obtaining data will be described. A numerical transport model has been used to simulate trajectories of a large number of infinitesimally small air parcels, or "synthetic" balloons. The output positions of these particles have been subject to further calculation to analyze the dispersion. The wind field data used as input data in the model have also been used externally to calculate kinetic energy spectra and second-order structure functions. This chapter will focus on the numerical model, but with the input data incorporated in that.

2.1 Model Description

The numerical model used in this thesis is the Lagrangian particle dispersion model FLEXPART (Stohl et al., 2005)[1]. The first version was made during the first author Andreas Stohl's military service of the Austrian Forces. Together with Stohl, it has been developed by people from Norwegian Institute for Air Research, Institute of Meteorology in Austria and Preparatory Commission for the Comprehensive Nuclear Test Ban Treaty Organization in Vienna, Austria. It is now used by a growing user community.

Originally, FLEXPART was made for calculating long-range and mesocale transport of air pollutants which origin were a point source, such as after an accident in a nuclear power plant. During years of expansion and adjustments, it has been generalized into a model concerning several subjects of atmospheric transport. At the present time, the main applications for the model are atmospheric transport of radionuclides after nuclear accidents, pollution transport, greenhouse gas cycles, stratosphere-troposphere exchange, water cycle research and others.

FLEXPART computes trajectories and concentrations of atmospheric tracer particles, not necessarily real particles, but infinitesimally small air parcels. Flexpart's main property is to simulate the long-range and mesocale transport, diffusion, convection, dry and wet deposition and radioactive decay of these. Compared to Eulerian models, the Lagrangian ones have

[1]See http://transport.nilu.no/flexpart for upgraded versions of the model description

no numerical diffusion. Another advantage is the independence of a computational grid, as the Eulerian ones have. In principle, the resolution of a Lagrangian model can be infinitesimally small. The tracers can be released from point, line, area or volume sources. The model can be used both forward in time to look on the dispersion of tracers from their sources, and backward in time to find a possible source contributor from a plume of tracers.

FLEXPART is an off-line model that most commonly uses meteorological fields from the ECMWF[2] numerical weather prediction model as input. These fields are forecast or analysis in gridded binary (GRIB) format on a latitude/longitude grid and on native ECMWF levels. Thus, to produce trajectories, the input velocity data are interpolated on the present particle position, i.e. on the Lagrangian grid, to advect the particle. The data can be global or only cover a limited area. A domain with higher resolution can also be nested into a mother domain. The input data have to contain five three-dimensional variables; horizontal and vertical wind components, temperature and specific humidity.

Since all three wind components are used to trace the particle path, the trajectories are three dimensional. This method of tracer tacking was suggested to be the most accurate by (Stohl and Seibert, 1998). Other error sources in the trajectory modeling are truncation errors, interpolation errors, inaccurate knowledge of the starting position and inaccuracies in the input wind fields.

The trajectory calculation in FLEXPART is based on the simple trajectory equation

$$\frac{\partial}{\partial t}\overrightarrow{X} = \overrightarrow{v}[\overrightarrow{X}(t)] \tag{2.1}$$

where t is time, $\overrightarrow{X}$ the position vector and $\overrightarrow{v} = \overrightarrow{\overline{v}} + \overrightarrow{v_t} + \overrightarrow{v_m}$ the wind vector. The latter is decomposed into a grid scale wind $\overrightarrow{\overline{v}}$, the turbulent wind fluctuations $\overrightarrow{v_t}$ and the mesocale wind fluctuations $\overrightarrow{v_m}$.

The turbulent motions $\overrightarrow{v_t}$, which are the small scale perturbations, are parameterized assuming a Markov process based on the Langevin equation (Thomson, 1987). This stochastic scheme is describing diffusive processes (*random walk motion*) as introduced in Chapter 3.3. However, the mesoscale motion $\overrightarrow{v_m}$ is not covered by this parameterization. For the part of the mesoscale not resolved by the grid scale wind, an independent Langevin equation for the mesoscale wind velocity fluctuations are solved based on the method of Maryon (1998). The idea is to assume that the variation of winds on the Eulerian input grid scale must be of a similar magnitude to the variation within a grid box.

[2]European Centre for Medium-Range Weather Forecasts

2.2 Model setup

In this thesis, the Flexpart model was used to calculate a large number of trajectories of infinitesimal small air parcels, so-called "synthetic" balloons. These were displaced around a latitude circle and then advected by the wind field of the ECMWF input data. As output was time series of all the particles positions.

The simulations are based on reanalysis data provided by ECMWF (ECMWF, 2002). These are produced through the latest reanalysis project of ECMWF, ERA-Interim (ECMWF, 2011). The data which are used have a horizontal resolution of $1^o \times 1^o$ and a 91 levels vertical resolution. The temporal resolution is three hours, where reanalysis at 00:00, 06:00, 12:00 and 18.00 UTC and forecast at intermediate times are used. Therefore, to yield output every hour, a time interpolation is done by the model.

16 model runs have been carried out. For one model simulation, 40000 particles were initially displaced uniformly around a latitude circle. Four different latitudes and two different altitudes are chosen to detect possible dispersion differences due to different dynamics at different atmospheric locations. It has been done two simulations for each location, one starting 00:00 UTC on the 1th of January and the other 00:00 UTC on the 1th of September, both in 2009. These extended for one month until 21:00 UTC on the 31th of January and the 30th of September respectively. The motivation for the latter is to detect possible seasonal variations. Because of this thesis' focus on general atmospheric dispersion properties, the choice of year is not of great importance. The model computes particle positions every hour. The output grid is $1^o \times 1^o$ with 3 vertical levels, since the motion on the scale of interest is assumed to be highly two dimensional. Chemical descriptions of neither the particles nor the atmospheric composition were needed for my purpose. Thus, all such settings were neglected in the model setup.

In addition to the use as the meteorological field in the model input, the ECMWF velocity data were used directly to calculate atmospheric kinetic energy spectra and structure functions. To obtain as much spatial scale information as possible, a $0.2^o \times 0.2^o$ horizontal resolution was used.

2.3 Lagrangian description

Flexpart uses the Lagrangian method to track particles. In the Lagrangian frame, every particle is marked by an "observer", continuously drifting with the particle from an initial state. It is illustrated by a balloon drifting with the winds, where the balloon represents a fluid particle. Thus in a model sense, a Lagrangian description yields a moving grid in time. In contrast, the Eulerian frame implies calculations on stationary grid points. The model input data, which moves the particle around by its meteorological wind field, is defined on such grid. Since the Eulerian

PARAMETER	VALUE
Model	FLEXPART
Type of model	Lagrangian particle dispersion model
Input data	ECMWF reanalysis
Particle release	Uniformly displaced around a latitude circle
Release latitudes	60S, 30S, 30 N and 60N
Release altitude	6km and 12km
Simulation start	01 January 2009 and 01 September 2009, 00:00 UTC
Simulation end	31 January 2009 and 31 September 2009, 21:00 UTC
Type of particle	General air parcel
Number of particles	40000
Grid resolution	$1^o \times 1^o$
Grid size	$360^o \times 180^o$
Output time step	3600s
Output fields	Particle positions in latitude/longitude[^{o}] and height[m]

Table 2.1: Input and output parameters for the FLEXPART model runs

grid is stationary, the wind velocities have to be interpolated on the model Lagrangian grid.

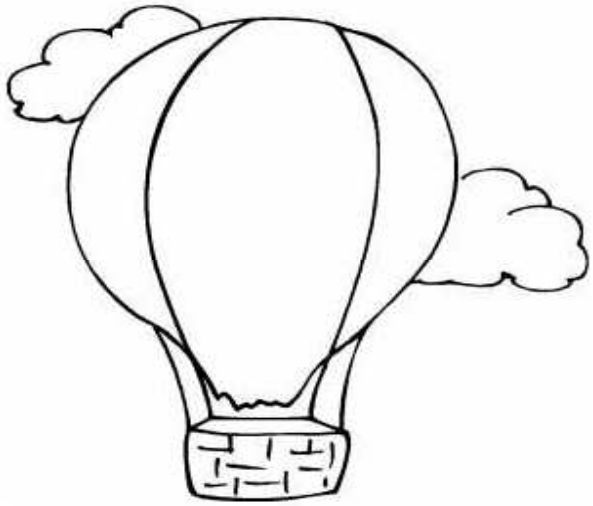

Figure 2.1: Description of the Lagrangian frame. A balloon drifts with the fluid motion. From *http://www.stuffintheair.com/the-hot-air-ballon.html*

Using a Lagrangian model is convenient when studying transport of atmospheric tracers. It allows us to follow each tracer particle, producing ensembles of particle trajectories. This forms a set of output data which can be analyzed using Lagrangian statistics. The latter is described in

Chapter 3. Another advantage by using a Lagrangian model follows naturally from the Lagrangian perspective. The nonlinear advection terms, causing an unclosed set of governing equation of the atmosphere (shown in Chapter 3.1), are included implicitly, without approximation (Wilson and Sawford, 1996).

2.4 Calculation

Here follows some important remarks according to the calculation of different parameters in this thesis.

- The model output yields particle positions in spherical coordinates. To obtain the separations between the particles, the arc length distance was calculated by the *swdist* function in MATLAB. There were not taking account for height, so the distances are actually calculated on the surface.

- There were also adopted some MATLAB functions in other calculations. A least square fit to the data was provided by using the *Regress* function. To obtain the probability density function of the data set separations, the *Hist* function was used. The kinetic energy spectrum was produced by the *Pwelch method* (Welch, 1967), which also is a function implemented in MATLAB. The method does a discrete Fourier transform on the ECMWF data to translate the spatial velocity field into a power field dependent on wavenumber.

Chapter 3

Theory

The scientific field of atmospheric turbulence includes flows of all temporal and spatial scales. This thesis, however, focuses on mesoscale turbulence which can be assumed to be quasi two dimensional (2-D). Thus, the theory introduced in this chapter is restricted to that range of scales. However, some features are general and will be considered very shortly first in this chapter. Then, it will be focused on two important turbulence models in 2-D theory, described by two distinct kinetic energy spectra. These form the framework for the main topic of this thesis, turbulent dispersion, which is systematically presented thereafter. After an introduction to absolute dispersion, predictions of relative dispersion and, in the last section, separation distributions are derived on the basis of 2-D turbulence theory.

3.1 The nature of turbulence

To illustrate one of the main concequences of turbulent motion, it is convenient to present the atmospheric momentum equation (Holton, 2004)

$$\frac{\partial}{\partial t}\overrightarrow{u} + \overrightarrow{u}\cdot\nabla\overrightarrow{u} + f\overrightarrow{k}\times\overrightarrow{u} = -\nabla(\frac{\overrightarrow{p}}{\overrightarrow{\rho}}) - \overrightarrow{g} \tag{3.1}$$

where $\overrightarrow{u}$ is the velocity field, f the Coriolis parameter, $\overrightarrow{p}$ the pressure field, $\overrightarrow{\rho}$ the density field and $\overrightarrow{g}$ the gravitational acceleration.

A sign of nonlinearity are terms containing products of dependent variables. Thus, $\overrightarrow{u}\cdot\nabla\overrightarrow{u}$ and $\nabla(\frac{\overrightarrow{p}}{\overrightarrow{\rho}})$ make the momentum equation nonlinear. To illustrate what these terms might cause, a simple nonlinear system, based on (Vallis, 2006), is used. That is

$$\frac{\partial}{\partial t}u + uu + ru = 0 \tag{3.2}$$

where r is some constant.

To include turbulence, the velocity u is decomposed into a mean and a fluctuating component.

$$u = \overline{u} + u' \tag{3.3}$$

where $\overline{u}$ is the mean velocity and u' the deviation from that mean.

The goal is to obtain a closed equation to predict the statistical behavior of the turbulence. Then, by substituting (3.3) into (3.2) and then averaging the equation leads to

$$\frac{\partial}{\partial t}\overline{u} + \overline{u}\overline{u} + r\overline{u} = 0 \tag{3.4}$$

$\overline{u}$ is simply $\overline{u}$ since $\overline{u'} = 0$. The problem appears due to the nonlinear term. That becomes

$$\overline{u}\overline{u} = \overline{(\overline{u} + u')(\overline{u} + u')} = \overline{(\overline{u^2} + 2\overline{u}u' + u'^2)} = \overline{u^2} + \overline{u'^2} \tag{3.5}$$

This term includes the mean of the correlation between the fluctuations, $\overline{u'^2}$, which is indeterminable. Thus, one needs an equation for $\overline{u}\overline{u}$. First multiplying (3.2) by u and then averaging yields

$$\frac{1}{2}\frac{\partial}{\partial t}\overline{u^2} + \overline{u}\overline{u}\overline{u} + r\overline{u^2} = 0 \tag{3.6}$$

This equation contains a new indeterminable term, $\overline{u}\overline{u}\overline{u}$. An equation for this cubic term will contain a quartic term, and so on in an infinite number of times, $\overline{u^n}$ requires $\overline{u^{n+1}}$. The equations are unclosed and there has to be made assumptions to close them. The density does not appear explicitly in the pressure coordinate version of (3.1), so a change of vertical coordinates eliminates the nonlinearity of that term (Holton, 2004). However, the nonlinearity of the advection term is not solved that elegantly. It is the source to the closure problem in the atmospheric momentum equation and needs to be represented in some way. Parameterizations have not been able to describe this term satisfactorily until now. It is not clear if it exists a useful closed-form solution of the equation at all.

The closure problem prevents the atmospheric governing equations being closed and hence solved exactly. It is a mathematical problem. In addition, the nonlinearity of (3.1) has some physical implications. It causes interactions among eddies of different length scales. By analyzing the nonlinear terms in the wavenumber space, it becomes clear that eddies, presented by wavenumbers, in groups of three are exchanging energy in so-called triad interactions (Vallis, 2006). There are two types of these interactions according to the length scale of the eddies which interact. By considering three arbitrary waves with wavenumber $\overrightarrow{k}$, $\overrightarrow{l}$ and $\overrightarrow{m}$, the two regimes are

- *Local interactions*, where waves of comparable sizes are interacting $\overrightarrow{k} \sim \overrightarrow{l} \sim \overrightarrow{m}$
- *Non-local interactions*, where waves of significantly different sizes are interacting $\overrightarrow{k} \sim \overrightarrow{l} >> \overrightarrow{m}$

The triad interactions are expressed through the advection term of (3.1). The same kind of terms appear in the continuity equation and the thermodynamic energy equation [1]. Then, the triads are responsible for a continuous transfer of momentum, mass and heat among different atmospheric scales. This is a fundamental consequence of the nonlinearity. Besides being a mathematical problem, nonlinearity is inherent in the physical system.

3.2 Two dimensional turbulence

The description in Section 3.1 is general and covers the main consequences of atmospheric turbulence. At small scales, particularly in the planetary boundary layer, the turbulence is three dimensional (3-D). The motion is influenced by interaction with the surface, which produce a strong vertical wind shear and therefore prevalent vertical mixing. On larger scales, due to the rotational earth and stratification, the two horizontal velocity components dominate over the vertical. Charney (1971) showed that under the quasi-geostrophic approximation, it is reasonable to assume the turbulence being approximately 2-D. This thesis follows Charney's argument and hence applies 2-D turbulence theory on the results in Chapter 5. Here follows a short introduction to this theory.

Since the triad interactions cause a transfer of momentum among eddy scales, the kinetic energy spectrum is appropriate to describe the turbulent flow field. To predict the Eulerian spectrum, there are first made some assumptions [2] (Vallis, 2006):

- Isotropy
- Homogeneity
- Stationarity

Homogeneity implies that turbulence has the same property, wherever in space. Then, analyzing turbulence in wavenumber space is sufficient. Stationarity means that the turbulence property is not changing in time. The isotropic assumption demands a turbulence which is the same in all direction. The kinetic energy spectrum in wavenumber space can then be written as

$$E(\overrightarrow{k}) = E(k) \tag{3.7}$$

where k is the wavenumber.

[1] See Holton (2004)

[2] Note that all assumptions are statistical

The previous and upcoming assumptions follow the arguments of Kolmogorov (1941), actually applied on a 3-D fluid. Batchelor (1953) and Fjørtoft (1953) showed almost simultaneously that energy is, opposite to 3-D turbulence, transferred to larger scales in 2-D turbulence, a so-called inverse energy cascade. One consequence is that kinetic energy is conserved. Although the direction of the energy transfer is opposite, Kraichnan (1967) inferred the same spectrum as for 3-D turbulence. A key assumption is to suppose a system, in which forcing and damping are happening at substantially different scales. Then, there exists a range of scales, which is only dominated by the nonlinear terms in the momentum equation in (3.1), i.e. by triad interactions causing energy transfer among eddies. This range is known as the *inertial range*. To ensure that forcing and damping are not dynamically important, the interactions between the eddies have to be local. Then, the flux of energy does only depend on processes ocurring near the scale of the interacting waves. This implies that the energy flux (energy per time) at a certain scale is only dependent on the energy on that scale, i.e. the energy spectrum, and the scale itself. Thus, the energy spectrum is proportional to ϵ and scale, represented by the wavenumber k. By imagining a situation where all scales have been energized through a spin-up period, the energy flux has to be constant to keep the spectrum stationary. Since kinetic energy per unit mass has units of $\frac{m^2}{s^2}$, the energy flux ϵ has units of $\frac{m^2}{s^3}$. The wavenumber has units of $\frac{1}{m}$. Then, by dimensional considerations, the energy spectrum ($\frac{m^3}{s^2}$) is

$$E(k) \propto \epsilon^{2/3} k^{-5/3} \tag{3.8}$$

which is the same spectrum as Kolmogorov (1941) predicted for a 3-D fluid.

Kraichnan (1967) suggested two inertial ranges in 2-D turbulence. Not only an upscale energy cascade could characterize the turbulent flow, but also an enstrophy transfer downscale, which caused an additional energy spectrum. Enstrophy is defined as

$$Z = \frac{1}{2}\zeta^2 \tag{3.9}$$

where ζ is the relative vorticity

Since vorticity is one over time, enstrophy has units of $\frac{1}{s^2}$. To infer an energy spectrum in the inertial range dominated by enstrophy transfer, exactly the same arguments apply as for the energy inertial range. The spectrum depends only on the rate of change of enstrophy, the enstrophy flux η, and scale k. The units of η has to be $\frac{1}{s^3}$. Then the shape of the spectrum is

$$E(k) \propto \eta^{2/3} k^{-3} \tag{3.10}$$

Then, the spectrum in the enstrophy range is steeper than that in the energy range. To see the dynamical differences between these two ranges, a closer view on the advecting time scales is convenient. The eddy interaction time scales have to depend solely on the energy (enstrophy) flux and scale under the local assumptions. Then, dimensional arguments show that for the energy range

$$T_{energy} \propto \epsilon^{-1/3} k^{-2/3} \tag{3.11}$$

while for the enstrophy range

$$T_{enstrophy} \propto \eta^{-1/3} \tag{3.12}$$

A fundamental difference between the two time scales is obvious. While the advecting time scale in the energy range depends on length scale, the corresponding time scale in the enstrophy range does not. The reason for this is that the triad interactions are local in the energy inertial range, while they are nonlocal in the enstrophy inertial range. Then, the size of the largest eddies characterizes the enstrophy transfer downscale in an enstrophy inertial range (see Section 3.1). That a local assumption causes a nonlocal spectrum sounds contradictory. However, it will be shown in Section 3.4 that the -3 power actually is in the limit between local and nonlocal turbulence and hence the spectrum describes so-called weakly nonlocal dynamics (Bennett, 1984).

By applying these two theoretical models on the mesoscale turbulence imposes some considerations about the scales of forcing (energy sources) and damping (energy sinks) in the atmospheric system. The radius of deformation[3] is suggested to be a scale, associated with a significant injection of kinetic energy (Salmon, 1980). How would a net upscale energy flux be satisfied in an inertial range at sub-deformation scales? By its huge amount of vorticity, the energy-containing eddies are also a source of enstrophy. Since enstrophy cascades towards smaller scales, a k^{-3} spectrum at atmospheric mesoscale is a reasonable suggestion[4]. Finally, it is being dissipated at some small scales. A consequence of that downscale enstrophy cascade is that enstrophy is not conserved in 2-D turbulence (Rhines, 1979). As will be shown, whether it is a k^{-3} or a $k^{-5/3}$ spectrum characterizing the turbulent flow is crucial on how particles disperse in 2-D turbulence.

3.3 An introduction to turbulent dispersion

The short introduction to 2-D turbulence theory in the previous section is a very useful tool both to understand but also interpret relative dispersion. It

[3]The scale where the flow is approximately balanced between the coriolis force and the pressure gradient force, i.e. geostrophic flow (Holton, 2004)

[4]Charney (1971) actually predicted a k^{-3} spectrum for quasi-geostrophic turbulence

will be shown that the particle separation growth depends on the turbulent cascade which dominates the flow. However, in some cases, turbulent motion can be explained in a fairly simple way. One example is the so-called *Random walk problem*. A lot of idealized cases could illustrate such motion, for instance perfectly drunk people walking from a bar. One basic result of the *Random walk problem* states that (Vallis, 2006)

$$<\mid D_n \mid^2>^{1/2}= \sqrt{n}s \tag{3.13}$$

where D_n is the position after n step and s is the length of each uniform step, which is uncorrelated with the previous one. Then (3.13) suggests that in a random walk, the root mean square displacement increases with the half-power of time.

3.3.1 Absolute dispersion

The *Random walk problem* does seem like an oversimplification of the nature. However, in some cases, it is a realistic description of how particles disperse. To formalize the random walk to a dispersion problem, it is convenient to introduce the single particle dispersion, or absolute dispersion. Based on the work of Taylor (1922) it is defined as

$$D_a(t) =<\mid x_i(t) - x_i(0) \mid^2> \tag{3.14}$$

where x denotes the position of a particle i at a time t. Thus, absolute dispersion describes how an ensemble of particles spread from their individual positions in time. It has been the most common way to statistically describe Lagrangian data (LaCasce, 2008b). Eddy heat fluxes and Rossby wave propagation are applications were single particle statistics have been applied. The following derivation comes from (LaCasce, 2008b)

To understand the behavior of dispersion in different time limits, diffusivity is a useful measure. The absolute diffusivity is defined as

$$K(t) = \frac{1}{2}\frac{d}{dt} < X^2 > \tag{3.15}$$

where X is the mean position vector of the particles. The constant appears due to the derivative of a squared variable. Thus, the absolute diffusivity is simply the time derivative of absolute dispersion. By applying the differentiation, (3.15) can be expressed as

$$K(t) =< u(t)X(t) >=< u(t) \int_0^t u(\tau)d\tau >= \int_0^t < u(t)u(\tau) > d\tau \tag{3.16}$$

which is the velocity autocorrelation. $u(t)$ can be inside the integral since the latter is with respect to the other time variable τ. If there is a stationary

velocity field, then

$$K(t) = \nu^2 \int_0^t R(\tau)dt \tag{3.17}$$

where

$$R(\tau) \equiv \frac{\int_0^t < u(0)u(\tau) > d\tau}{\nu^2} \tag{3.18}$$

is the normalized velocity autocorrelation and ν^2 is the velocity variance of the particles. The stationarity is reflected by the substitution of $u(0)$ for $u(t)$ in (3.18).

To study the short time limit behavior ($t \rightarrow 0$), it is convenient to expand the autocorrelation in a Taylor series.

$$R(\tau) = 1 + \frac{dR}{dT}t + ...O(t^2) \tag{3.19}$$

and

$$lim_{t\rightarrow 0}R = 1 \tag{3.20}$$

Then, using (3.17),

$$lim_{t\rightarrow 0}K = \nu^2 \int_0^t 1dt = \nu^2 t \tag{3.21}$$

Then, by integration, this implies that absolute dispersion grows quadratically in time in the short time limit.

In the long time limit, since they are far apart, it is realistic to assume that the velocities become uncorrelated. Then

$$lim_{t\rightarrow \infty}R = 0 \tag{3.22}$$

and

$$lim_{t\rightarrow \infty}K = \nu^2 \int_0^t 0dt = const. \tag{3.23}$$

The diffusivity converges to a constant in the long time limit. This is called a *diffusive* process and the diffusion equation can describe the motion. In this range, the dispersion must grow linearly in time. This is exactly the same growth as in the *Random walk problem*. Thus, in some cases, though not focused on in this thesis, this simple situation is sufficient to describe a turbulent flow.

3.4 Relative dispersion

Absolute dispersion characterizes the mean flow, since all the single fluid motions are averaged at each time step. Thus absolute dispersion reflects the mean drift of the cloud and the spread about the instant mean position. Spreading due to deviations from the mean flow is not described, reflecting the limitation of single particle statistics. A more proper description of a tracer cloud should also include additional flow fields, which are necessary to extend the physical applicability. By considering the time evolvement of the separations between particles, relative dispersion satisfies that requirement. Inherent in this measure, there is a property of distinguishing different kind of flows. For this reason, relative dispersion is related to the turbulent models in Section 3.2, which was shown to cause a transfer of momentum among different scales of motion. This connection comes automatically from the following derivations, which follow those of LaCasce (2008a) and Bennett (1984). Relative dispersion, or two particle dispersion, is defined as

$$D_r(t) = <\mid x_i(t) - x_j(t) \mid^2> \tag{3.24}$$

where i and j denote two particles and x their position.

As for single particles, the diffusivity can be defined. Relative diffusivity is expressed as

$$K(t) \equiv \frac{1}{2}\frac{d}{dt}\overline{r^2} = \overline{rv} = \overline{r_0 v} + \int_{t_0}^{t} \overline{v(t)v(\tau)d\tau} \tag{3.25}$$

where r is the distance between the particles, v the separation velocity and r_0 the initial separation.

The first term on the right hand side denotes the correlation between the initial separation of the pairs and their separation velocities. It is often assumed to be vanishingly small when there is a large ensemble of pairs (LaCasce, 2008a). However, in the short time limit, it is convenient to assume that the particles are close to each other. Then their velocity difference is approximately constant and the separations grow linearly in time. Then, from (3.25)

$$K \propto t \tag{3.26}$$

Thus, the relative dispersion grows quadratically in the short time limit.

The second term in (3.25) is the time integral over the velocity cross correlation. It describes the correlation between the separation velocity at time t with previous separation velocities at time τ. This term does only dominate when the particle's "memory" of their initial state is lost, i.e. $\overline{y_0 v} \to 0$. It

can be rewritten to yield

$$\int_0^t \overline{v(t)v(\tau)}d\tau = \int_0^t \overline{(u_i(t) - u_j(t))(u_i(\tau) - u_j(\tau))}d\tau \tag{3.27}$$

where u is the particles' velocities. Since the turbulence is homogeneous,

$$\overline{u_i(t)u_i(\tau)} = \overline{u_j(t)u_j(\tau)} \tag{3.28}$$

then,

$$\begin{aligned}\int_0^t \overline{v(t)v(\tau)}d\tau &= 2\int_0^t \overline{u_i(t)u_i(\tau)}d\tau - 2\int_0^t \overline{u_i(t)u_j(\tau)}d\tau \\ &= 2K_a(t) - 2\int_0^t \overline{u_i(t)u_j(\tau)}d\tau \end{aligned} \tag{3.29}$$

where K_a is the absolute diffusivity from (3.16)

In the long time limit, when the velocities of the two particles are assumed to be uncorrelated, the second term in (3.29) goes to zero. Then, the relative diffusivity converges to twice the absolute diffusivity. Therefore, after sufficiently long time, the relative dispersion also behaves like a simple random walk problem.

At intermediate times, it is useful to consider the second order structure function, which is simply the mean square Lagrangian velocity difference. For a homogeneous flow, it is the same as the Eulerian difference (Bennett, 1984).

$$\overline{v(r)^2} = \overline{(u(x+r,t) - u(x,t))^2} = 2\int_0^\infty E(k)[1 - J_0(kr)]dk \tag{3.30}$$

where $E(k)$ is the kinetic energy spectrum and J_0 the zero-order Bessel function of the first kind. It appears due to the distance r between the particles. If r goes to zero, i.e. two particles collapse to a single particle, $[1 - J_0(kr)]$ goes to zero. In this sense, it is a distance weighting function for the kinetic energy spectrum $E(k)$ for each k. It is expressed as

$$1 - J_0(kr) \approx \begin{cases} \frac{1}{4}k^2r^2, kr \ll 1, \\ 1 + O(kr)^{-1/2}, kr \gg 1 \end{cases} \tag{3.31}$$

Consider a subrange in which the turbulent flow is stationary, i.e. $E \propto k^{-\alpha}$ (Section 3.2). The pair separation r is in this subrange. Then, by using (3.31)

$$\begin{aligned}\overline{v(r)^2} &\approx 2\int_0^{1/r} k^{-\alpha}(\frac{1}{4}k^2r^2)dk + 2\int_{1/r}^\infty k^{-\alpha}dk \\ &= \frac{1}{2}r^2\frac{1}{3-\alpha}k^{3-\alpha}\,|_0^{1/r} + \frac{2}{1-\alpha}k^{1-\alpha}\,|_{1/r}^\infty \end{aligned} \tag{3.32}$$

where the first term on the right hand side expresses the influence from eddies larger than the separation r ($k < 1/r$) and the second term expresses the influence from eddies smaller than the separation ($k > 1/r$). The latter diverges for $\alpha \leq 1$ when $k \to \infty$. The structure function is then dominated by the energy from the smallest eddies. These are not able to spread particles with substantially larger separations from each other, so this case implies absolute dispersion. The two following cases consider relative dispersion under the two different turbulent cascades presented in Section 3.2. First, the local Kolmogorov spectrum is applied.

3.4.1 Local dispersion

If $1 < \alpha < 3$, both terms on the right hand side of (3.32) converge when $k \to 0$ and $k \to \infty$. Then, both the largest and the smallest eddies of the range do not influence the structure function. Thus the dispersion has to be dominated by the eddies on the same scale as r. The dispersion is local, similar to the triads when eddies with comparable sizes interact (Section 3.1). Then from (3.32)

$$\overline{v(r)^2} \propto r^{\alpha-1} \tag{3.33}$$

and hence the separation velocity can be expressed as

$$\overline{v(r)} \propto r^{\frac{\alpha-1}{2}} \tag{3.34}$$

Then, from (3.25), the corresponding diffusivity scales as [5]

$$K = \frac{1}{2}\frac{d}{dt}\overline{r^2} \propto vr \propto r^{(\alpha-1)/2} r \propto r^{(\alpha+1)/2} \tag{3.35}$$

In Section 3.2, it was shown that the local energy spectrum has the $k^{-5/3}$ shape (Kolmogorov, 1941). Then, with $\alpha = 5/3$, the diffusivity scales as

$$K \propto r^{(\frac{5}{3}+1)/2} \propto r^{4/3} \tag{3.36}$$

This is what Richardson (1926) observed and is therefore often called "Richardson's 4/3-law". Since the dispersion at intermediate scales can be determined by the inertial range flow, in this case an inverse energy cascade, it can be assumed a dependence solely on scale (m) and the energy flux $\epsilon(\frac{m^2}{s^3})$. Then the relative diffusivity $K(\frac{m^2}{s})$, scales as

$$K \propto \epsilon^{1/3} r^{4/3} \tag{3.37}$$

The corresponding dispersion is [6]

[5] (Bennett, 1984) showed this in a proper way

[6] A more formal derivation of the Richardson dispersion is done by deducing it from the corresponding separation distribution. See Section 5.1

$$\overline{r^2} \propto \epsilon t^3 \tag{3.38}$$

Thus, in an energy inertial range, dispersion grows as time cubed. This is often called Richardson dispersion.

3.4.2 Nonlocal dispersion

The first term on the right hand side of (3.32) diverges for $\alpha \geq 3$ when $k \to 0$. Then the structure function is controlled by the largest energy-containing eddies of the range. According to Section 3.2, the dispersion is therefore nonlocal.

First consider the strictly nonlocal case $\alpha > 3$. Then, from (3.32)

$$\overline{v(r)^2} \approx \frac{1}{2} r^2 \int k^{-\alpha} k^2 dk = \frac{1}{2} r^2 \int k^2 E(k) dk = c\Omega r^2 \tag{3.39}$$

where

$$\Omega = \int k^2 E(k) \tag{3.40}$$

is the total enstrophy.

In the limit $\alpha \to 3$, it is clear that the local form of the structure function (3.33) matches the nonlocal form (3.39). This shows that an enstrophy cascading inertial range, i.e. a turbulent flow characterized by a k^{-3} kinetic energy spectrum, is valid under the local assumption (Section 3.2).

For $\alpha = 3$, under so-called weakly nonlocal dynamics, the relative diffusivity scales as

$$K \propto \overline{r^2} \tag{3.41}$$

In accordance with the local assumption in Section 3.2, the diffusivity has to depend, in addition to distance, on the enstrophy flux η ($\frac{1}{s^3}$). Thus, dimensional arguments yield

$$K \propto \eta^{1/3} r^2 \tag{3.42}$$

Then the relative dispersion is [7]

$$\overline{r^2} \propto exp(C\eta^{1/3} t) \tag{3.43}$$

where C is some constant due to intergration

[7] This can also be deduced more properly from the Lundgren distribution. See Section 3.5.3.

The corresponding enstrophy cascade time scale is therefore

$$T \propto \eta^{-1/3} \tag{3.44}$$

which is in accordance with the enstrophy cascade time scale detected in Section 3.2.

The expression in (3.43) is sometimes called "Lin's law" after (Lin, 1972) which predicted this. In the enstrophy cascade, separation of pairs are growing exponentially in time with a growth rate determined by the largest eddies of the flow. However, for strongly nonlocal dynamics ($\alpha > 3$), the form of (3.39) yields the same scaling properties for diffusivity as for $\alpha = 3$. Thus the dispersion is growing exponentially for all $\alpha \geq 3$. Then, observing exponential dispersion does only imply nonlocal dispersion, not necessarily an inertial enstrophy range. Additional information about the background flow is needed.

3.5 Probability density functions

Basic theory of statistics implies that relative dispersion is simply the variance of the separation distribution. The variance is the second order moment of the probability density function (PDF). This moment describes the mean width of the distribution and can obviously not describe the full distribution alone. Thus some important information is lost when only relative dispersion is considered. The fourth order moment kurtosis indicates the shape of the PDF and could be a better tool to distinguish different dispersion regimes. However, as will be shown in Chapter 5, the kurtosis has often a noisy behavior. The distribution itself has also been used to detect the relative dispersion, e.g. by LaCasce (2010), who examined separation PDFs for one atmospheric (EOLE), two oceanic (SCULP and POLEWARD) and one numerical data set. The results were shown to be more conclusive than the moments provided. In the following sections, the PDFs for the different turbulent predictions given in Section 3.4 are presented. The derivations come from Bennett (1984), Bennett (2006) and LaCasce (2010).

3.5.1 The Fokker-Planck equation

To achieve an analytical solution for separation PDFs of different turbulent regimes, a Fokker-Planck equation (FP) was proposed by Richardson (1926).

$$\frac{\partial}{\partial t}p = \frac{1}{r}\frac{\partial}{\partial r}(\kappa_2 r \frac{\partial}{\partial r}p) \tag{3.45}$$

where $p = p(r,t)$ is the probability density function, r is the pair separation and κ_2 the (longitudinal) relative diffusivity.

To obtain an unique solution for (3.45), two boundary conditions and one initial condition for P are required. From Bennett (1984), suitable conditions are

$$r\kappa\frac{\partial}{\partial r}p \rightarrow 0 \text{ as } r \rightarrow 0,\ \infty \tag{3.46}$$

and

$$p(r,0) = \frac{1}{2\pi r}\delta(r - r_0) \tag{3.47}$$

where δ is the Dirac delta function. Reminding the properties of the δ-function, this initial condition suggests that all the particle pairs have the same initial separation.

The pre-factor $\frac{1}{2\pi r}$ in (3.47) both insures a normalized distribution and the isotropic assumption since

$$\int_0^{2\pi}\int_0^{\infty} prdrd\theta = 2\pi\int_0^{\infty} prdr = 1 \tag{3.48}$$

where 2π comes from the integration over all angles θ in the 2-D space.

3.5.2 Richardson distribution

To obtain a PDF for a Richardson distribution, it is convenient to assume a relative diffusivity based on "Richardson's law" deduced in Section 3.4.1. Then, the longitudinal diffusivity is (Bennett, 2006)

$$\kappa_2 = \beta r^{4/3} \tag{3.49}$$

From dimensional arguments, β has to scale as $\frac{m^{2/3}}{s}$. Since the energy flux scales as $\frac{m^2}{s^3}$, this is related to β by

$$\beta \propto \epsilon^{1/3} \tag{3.50}$$

The particular solution of (3.45) is obtained via the Laplace transform. The version for 2-D turbulence is (LaCasce, 2010)

$$p(r,t) = \frac{3}{4\pi\beta t r_0^{2/3} r^{2/3}} exp(-\frac{9(r_0^{2/3} + r^{2/3})}{4\beta t}) I_2(\frac{9 r_0^{1/3} r^{1/3}}{2\beta t}) \tag{3.51}$$

where r_0 is the initial separation and I_2 is the modified Bessel function of second order.

The moment of order n is expressed by

$$< r^n >= 2\pi\int_0^{\infty} r^n p(r) r dr = 2\pi\int_0^{\infty} r^{n+1} p(r) dr \tag{3.52}$$

The kurtosis is obtained by using the definition based on the raw moment. That is

$$Ku = \frac{< r^4 >}{(< r^2 >)^2} \tag{3.53}$$

The raw moments of the Richardson PDF are derived throughout the work with this thesis. Consequently, it is shown in the result chapter, i.e. Chapter 5.

3.5.3 Lundgren distribution

In the nonlocal inertial range dominated by an entrophy cascade, it was shown that the relative diffusivity scales as (Section 3.4.2)

$$\kappa_2 \propto \eta^{1/3} r^2 = \frac{r^2}{T} \tag{3.54}$$

where

$$T \propto \eta^{-1/3} \tag{3.55}$$

is the enstrophy cascade time scale, determined by the largest eddies of the flow. The solution of (3.45) with the same initial and boundary conditions was obtained by Lundgren (1981).

$$p(r) = \frac{1}{4\pi(\pi t/T)^{1/2} r_0^2} exp(-\frac{[ln(r/r_0) + 2t/T]^2}{4t/T}) \tag{3.56}$$

The corresponding raw moments [8] of the distribution, are deduced from (3.52).

$$< r^n >= r_0^n exp(\frac{n(n+2)t}{T}) \tag{3.57}$$

The second order raw moment, relative dispersion (n=2), is then

$$< r^2 >= r_0^2 exp(\frac{8t}{T}) \tag{3.58}$$

and by applying (3.53), the fourth order raw moment, kurtosis (n=4), is

$$Ku = exp(\frac{8t}{T}) \tag{3.59}$$

[8] Since separations are positive definite, it is preferable to derive the raw moments (LaCasce, 2010)

Thus, the exponential growth of pair separations in the enstrophy range is also obtained by deriving the raw moments of the probability density functions. As the variance, the kurtosis is exponential, implying that the Lundgren PDF is not self-similar. A self-similar distribution has constant kurtosis. This provides a tool to distinguish exponential non-local dispersion from local Richardson dispersion. The latter is shown to be self-similar in the asymptotic limit, i.e. during t^3 growth of the relative dispersion.

3.5.4 Rayleigh distribution

In Section 3.4, it was shown that relative dispersion grows linearly in time in the long time limit. This is when the pair velocities are uncorrelated. The relative diffusivity is constant and twice the absolute diffusivity and hence behaves like a *random walk problem*. The solution of the FP equation (3.45) is then (LaCasce, 2010)

$$p(r,t) = \frac{1}{4\pi\kappa_2 t} exp(-\frac{r_0^2 + r^2}{4\kappa_2 t}) I_0(\frac{r_0 r}{2\kappa_2 t}) \tag{3.60}$$

where I_0 is a modified Bessel function of order zero.

Since the pair velocities are more likely to be uncorrelated after long time, it is preferable to study the asymptotic limit ($r >> r_0, \beta t >> r$). Then (3.60) reduces to

$$p(r,t) = \frac{1}{4\pi\kappa_2 t} exp(-\frac{r^2}{4\kappa_2 t}) \tag{3.61}$$

which is proportional to the Rayleigh distribution (Papoulis, 1991).

Utilizing (3.52) (3.53) provide the raw moments. The relative dispersion is then

$$< r^2 >= 4\kappa_2 t \tag{3.62}$$

and the kurtosis is

$$Ku_{Ra} = 2 \tag{3.63}$$

Then, from probability density functions, it is also observed that the pairs undergo a diffusive process after sufficiently long time. The Rayleigh distribution is also self-similar.

Chapter 4

Previous studies

Due to the economic extent of large balloon projects, there have only been a few observational studies on relative dispersion in the atmosphere. Therefore, and since these are relevant, oceanic studies on relative dispersion have to be considered. As shown in the previous chapter, the Eulerian kinetic energy spectrum reflects the turbulent flow, which in turn determines the relative dispersion in 2-D turbulence theory. Thus, studies which interpret kinetic energy spectra are important contributors to the understanding of turbulent advection of tracer particles. This short chapter covers some important studies connected to this issue and emphasizes the contradicting conclusions among some of these. In Chapter 5, this thesis' results are discussed against some of the studies presented here. Table (4) summarizes some relevant findings, both in theoretical and observational studies.

Richardson (1926) studied smoke plumes spreading from factory stacks and observed that the rate of cloud dispersion increased with the size of the cloud. Richardson realized that the diffusivity was dependent on scale to the 4/3-power. This relation is known as Richardson's law. It was deduced for a 3-D flow, as in the planetary boundary layer, but as shown in Chapter 3.4.1, the law is also consistent with 2-D turbulence theory. It implies cubic growth of the relative dispersion.

From the 1970's, there have been two major balloon projects in the atmosphere, EOLE and TWERLE. The former was performed during a one year period from August 1971 until July 1972 in the Southern hemisphere (Morel and Bandeen, 1973). It included 480 balloons released and floated at approximately the 200hPa level. Morel and Larcheveque (1974) (ML) examined these data and the results are shown in Figure 4.1. It displays exponentially growing dispersion from 100 km up to 1000km, about the radius of deformation. The flow was approximately isotropic at the same range of scales, so the theory described could be implemented. Beyond 1000km, the dispersion develops into a diffusive one, with linear growth. However this range of scales is zonally anisotropic, so applying 2-D theory needs to be done carefully.

The other balloon project, TWERLE (Tropospheric Wind Earth Radio Location Experiment), captured data from June 1975 to August 1976 (Jullian

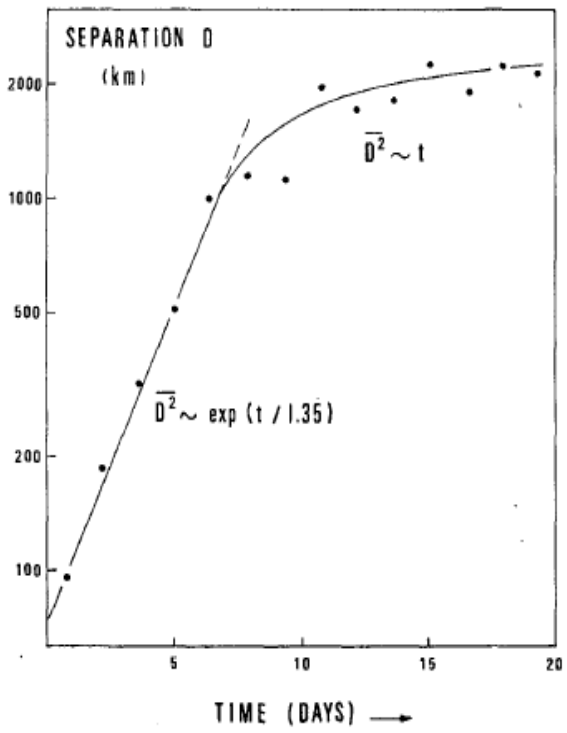

Figure 4.1: Root mean square distance vs. time for the EOLE balloon pairs. From Morel and Larcheveque (1974)

et al., 1977). These were also released in the Southern hemisphere and the 393 balloons floated at approximately 150hPa. The data were examined by Er-El and Peskin (1981) (EP) and their relative dispersion results are shown in Figure (4.2). As ML, they found evidence for exponential growth of separations below the deformation radius. In addition, EP calculated the fourth order moment of the separation distribution, the kurtosis (see Chapter (3.5)), but only at one time. A time series is necessary to infer the evolvement of the dispersion, though, the kurtosis value of 7.02 in the subtropics at least indicated a strongly non-Gaussian separation distribution. However, it does not rule out neither Richardson nor exponential growth. This study also included a comparison between high and low latitudes, but no obvious differences were found. At large scales, a superdiffusive regime was detected, i.e. power law growth faster than linear.

Although two balloon experiments were consistent with each other, it is still not clear how dispersion behaves at sub-deformation scales. ML also examined relative velocities' dependence on separations. The measures suggested Richardson behavior rather than exponential dispersion. Both the EOLE and TWERLE data are noisy, so a power law might fit equally well as an exponential. Lacorata et al. (2004) re-examined the EOLE balloon data using another method, Finite Scale Lyapunov Exponent (FSLE). The motivation for this method is to distinguish the spatial scales from

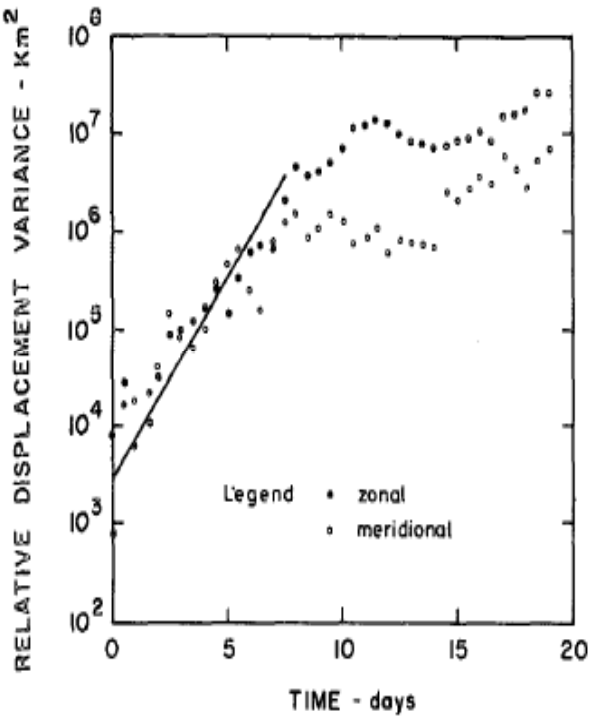

Figure 4.2: Dispersion vs. time for the TWERLE balloon pairs. From Er-El and Peskin (1981)

each other[1]. A fundamental problem with relative dispersion is the time-based average, which makes it inconclusive after only a few days (LaCasce, 2010). Dispersion from flows covering a wide range of scales are averaged. Lacorata et al. (2004) found only exponential growth below 100km. Between 100km and 1000km, Richardson dispersion was detected. LaCasce (2010) used probability density functions (PDF) of the relative displacements to analyze the relative dispersion of the EOLE data set. While the PDFs were consistent with the Lundgren distribution, indicating exponential dispersion up to 100-200km, behavior beyond these scales was hard to detect. What might be a problem is the unstable statistics caused by too few pairs, though this study included so-called *chance pairs*. These method using *chance pairs* picks out particles which float near each other a time after deployment. The statistics are more robust (LaCasce, 2010), but it has been discussed if these produce relative dispersion with unwanted features.

Since atmospheric dispersion is related to the atmospheric kinetic energy spectra (Section 3.4), this can be a useful interpretation tool in addition to PDFs and dispersion themselves. Nastrom and Gage (1984) (NG) used velocity data at the tropopause from 7000 commercial aircrafts over US to calculate a kinetic energy spectrum. The results are shown in Figure (4.3). Here, a k^{-3} enstrophy range is detected from wavelengths at some hundred kilometers up to thousands of kilometers, while a $k^{-5/3}$ energy range

[1]The method is described by Lacorata et al. (2004)

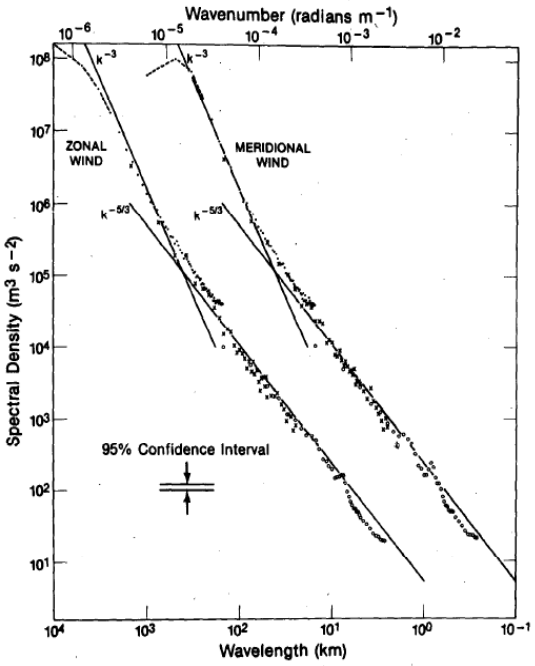

Figure 4.3: Kinetic energy spectra from data collected on commercial airplanes over U.S. Both zonal and meridional components are shown, with the latter shifted one decade to the right. From Gage and Nastrom (1986)

is present at smaller scales. A comparison between location (latitude, stratosphere vs. troposphere) and season was included, but the slope was shown to be universal. Since the lower x-axis displays wavelengths and the pair separation scale is considered as an eddy radius, a multiplication by a quarter is convenient. In light of this, the energy spectrum supports ML and EP. The scales displaying a Kolmogorov spectrum might indicate flows at such small scale that it is a subject to three-dimensional turbulence. Cho and Lindborg (2001) (CL) considered structure functions in the troposphere and the stratosphere. As shown in Section (3.4), relative dispersion derives directly from the second-order structure function, so in that sense, the latter is a more proper tool than the kinetic energy spectrum. CL suggested an energy range at the smallest scales (2km-20km) taken over by an enstrophy range. This is in line with GN. CL also inferred a clearer r^2-range in the stratosphere than in the troposphere, though, the reason for this is unclear.

On the basis of these studies, the question may arise if seasonal and geographical variations could affect the dispersion characteristics. Huber et al. (2001) used ECMWF reanalysis data to advect particles on isentropic surfaces. Two distinct mixing regimes were detected, one for the tropical, which supported exponential growth, and one for the extratropical region, which supported power-law growth. The latter was mainly ballistic, i.e. t^2 growth. This systematic study did also compare two seasons (the boreal winter and summer), two heights (the 315K and 330K isotropic surfaces) and 72 regions of particle initializations. In addition to the distinct dis-

persion differences between the extratropics and the tropics, there were only small deviations within these regions. The exception was the somewhat stronger mixing ($\simeq t^3$) at some locations in the Northern hemispheric winter due to a more pronounced wave-though pattern. Differences with height were hardly detectable. These results do rely heavily on isentropic conditions, which is reasonable to assume in the extratropics. However, the resolution of the input velocity field ($2.5^o \times 2.5^o$ horizontal grid) limits the reliability of the small scale dispersion. Another important aspect regarding the results here is that Huber et al. (2001) based their conclusion on a 10 days fit of the relative dispersion.

There have been paid increasingly attention to oceanic projects during the last decade. The use of drifters and floats to make Lagrangian trajectories are much easier and less expensive than launching balloons in the atmosphere. Ollitrault et al. (2005) found exponential growth at subdeformation scales in the Gulf of Mexico, Koszalka et al. (2009) did the same in the Nordic Sea. These results are important contributions to understand the large scale turbulence in the atmosphere, which is in lack of observational results since ML and EP examined the EOLE and TWERLE projects.

The reason for this study is to improve the understandings of the mesoscale dispersion on the basis of the aforementioned studies. Motivated by Huber et al. (2001), different heights, seasons and latitudes will be compared. However, this study is limited to the extratropics. Since all the particles are deployed at the same time around a latitude circle, no zonal dependence will be inferred. The use of a numerical model provides build-in limitations on both temporal and spatial resolution, i.e. describing the exact particle motion. However, a huge amount of particles are possible, which yields a more stable statistics.

YEAR	PROGRESS
1926	L.F.Richardson inferred empirically a power-law correlation for the relative diffusion, which corresponds to cubic growth for the relative dispersion
1941	A.N.Kolmogorov suggested a $k^{-5/3}$ dependence of the energy spectrum in an energy cascading inertial range
1953	G.K.Batchelor and R.Fjørtoft independently inferred an inverse energy cascade in an inertial range in 2-D turbulence
1967	R.H.Kraichnan asserted that there must be two inertial ranges in two-dimensional turbulence: One characterized by an energy cascade ($k^{-5/3}$), the other by an enstrophy cascade (k^{-3})
1971	J.G Charney showed that the theory of 2-D turbulence could be utilized on quasi-geostrophic turbulence
1971	J.Lin suggested an exponential dependence of the relative dispersion in an enstrophy-cascading inertial range
1974	P.Morel and M.Larcheveque studied balloon data at 200mb from the EOLE project in the Southern hemisphere. Exponential separation growth was detected. Lacorata et al. (2004) and LaCasce (2010) reexamined the data by different methods, FSLE and separation PDFs respectively. The results were contradicting
1981	J.Er-El and R.L.Peskin found exponential separation growth for balloon data at 150mb captured by the TWERL experiment
1985	K.S.Gage and G.D.Nastrom used velocity data from commercial aircrafts to infer the atmospheric kinetic energy spectrum. An energy range at small wavelengths was taken over by an enstrophy range above a few hundred kilometers. Cho and Lindborg (2001) used structure functions to infer the same, an enstrophy cascade below the deformation radius
2003	J.H.LaCasce and Ohlmann examined surface drifters in the Gulf of Mexico and detected exponential growth of the relative dispersion at sub-deformation scales(LaCasce and Ohlmann, 2003). (Ollitrault et al., 2005; Koszalka et al., 2009) support these findings through projects in the Eastern Atlantic and the Nordic Seas respectively.

Table 4.1: A list of some relevant findings in 2-D turbulence theory and in Lagrangian and Eulerian observations

Chapter 5

Results

In this chapter, the results, motivated by the goal of this thesis, are presented. First, the moment of the full Richardson distribution is derived for later comparisons with the data. Then follow the results based on several FLEXPART model runs. A discussion of the theoretical assumptions made is given, with emphasis on isotropy. Thereafter, relative dispersion and probability density functions of the distributions are illustrated on several figures. Comparisons both among the data sets produced here and with the renewed EOLE data set by LaCasce (2010) are done. To figure out the dispersion characteristics, theoretical predictions derived in Chapter 3 are also shown. The choice of locations, i.e. altitude and latitude, and season, is based on observed features through this work. For an extended interpretation, second-order structure functions from the ECMWF reanalysis wind data are shown finally.

5.1 The moments of the full Richardson distribution; a derivation

The motivation behind this derivation was to obtain a value of β to provide the full Richardson distribution in Section 5.5.2 later in this chapter. A fit with this function would eventually suggest Richardson dispersion, so it could be crucial for the main conclusion of this thesis.

The 3-D variant of the full Richardson was derived by Bennett (1984). While Richardson (1926) only provided an asymptotic 2-D distribution, LaCasce (2010) derived the full solution in 2-D. This is given by (3.51) in Chapter 3.5. A substitution into the definition of the moment, expressed by (3.52), yields

$$\begin{aligned} < r^n > &= 2\pi \int_0^\infty r^{n+1} \frac{3}{4\pi\beta r_0^{2/3} r^{2/3}} exp(-\frac{9(r_0^{2/3} + r^{2/3})}{4\beta t}) I_2(\frac{9 r_0^{1/3} r^{1/3}}{2\beta t}) dr \\ &= \frac{3}{2\beta t r_0^{2/3}} exp(-\frac{9 r_0^{2/3}}{4\beta t}) \int_0^\infty r^{(3n+1)/3} exp(-\frac{9 r^{2/3}}{4\beta t}) I_2(\frac{9 r_0^{1/3} r^{1/3}}{2\beta t}) dr \\ &= C(t) \int_0^\infty r'^{(3n+2)/2} exp(-\frac{9r'}{4\beta t}) I_2(\frac{9 r_0^{1/3} \sqrt{r'}}{2\beta t}) dr' \end{aligned} \tag{5.1}$$

where it is done a substitution $r' = r^{2/3}$, which yields

$$dr = \frac{3}{2} r^{1/3} dr' \tag{5.2}$$

The constant factor C is defined as

$$C(t) \equiv (\frac{3}{2})^2 \frac{1}{\beta t r_0^{2/3}} exp(-\frac{9 r_0^{2/3}}{4\beta t}) \tag{5.3}$$

To solve the integral in (5.1), an integral identity from (Gradshteyn and Ryzhik, 1980) is used. That is

$$\int_0^\infty x^{\mu-\frac{1}{2}} exp(-\alpha x) I_{2\nu}(2\gamma\sqrt{x}) dx = \frac{\Gamma(\mu+\nu+\frac{1}{2})}{\Gamma(2\nu+1)} \gamma^{-1} exp(\frac{\gamma^2}{2\alpha}) \alpha^{-\mu} M_{-\mu,\nu}(\frac{\gamma^2}{\alpha}) \tag{5.4}$$

where

$$\Gamma(n) = (n-1)! \tag{5.5}$$

is the Gamma function and $M_{-\mu,\nu}(\frac{\beta^2}{\alpha})$ is the Whitakker M Function. The latter is defined as (Abramowitz and Stegun, 1972)

$$M_{-\mu,\nu}(z) = exp(-\frac{1}{2}z) z^{\frac{1}{2}+\nu} M(\frac{1}{2}+\nu+\mu, 1+2\nu, z) \tag{5.6}$$

where M is Kummer's Function.

For this case, the symbols in (5.4) and (5.6) have to be defined as

$$\mu = \frac{3n+3}{2}, \alpha = \frac{9}{4\beta t}, \nu = 1, \gamma = \frac{9 r_0^{1/3}}{4\beta t} z = \frac{\gamma^2}{\alpha} \tag{5.7}$$

Then,

$$
\begin{aligned}
< r^n > &= K(t)\frac{\Gamma(\frac{3n+3}{2}+1+\frac{1}{2})}{\Gamma(3)}(\frac{9r_0^{1/3}}{4\beta t})^{-1}(\frac{9}{4\beta t})^{-(\frac{3n+3}{2})}exp(\frac{9r_0^{2/3}}{8\beta t}) \\
&\quad M_{(\frac{3n+3}{2}),1}(\frac{9r_0^{2/3}}{4\beta t}) \\
&= (\frac{3}{2})^2\frac{1}{\beta t r_0}(\frac{4\beta t}{9})^{(\frac{3n+3}{2})+1}\frac{\Gamma(\frac{3n+6}{2})}{\Gamma(2)}exp(-\frac{9r_0^{2/3}}{8\beta t}) \\
&\quad M_{-\frac{3n+3}{2},1}(\frac{9r_0^{2/3}}{4\beta t}) \\
&= \frac{1}{2r_0}\frac{4\beta t}{9})^{(\frac{3n+3}{2})}\Gamma(\frac{3n+6}{2})exp(-\frac{9r_0^{2/3}}{8\beta t})exp(-\frac{9r_0^{2/3}}{8\beta t}(\frac{9r_0^{2/3}}{4\beta t})^{\frac{3}{2}} \\
&\quad M(\frac{6+3n}{2},3,\frac{9r_0^{2/3}}{4\beta t}) \\
&= \frac{1}{2}\Gamma(\frac{3n+6}{2})(\frac{4\beta t}{9})^{\frac{3n}{2}}exp(-\frac{9r_0^{2/3}}{4\beta t})M(\frac{6+3n}{2},3,\frac{9r_0^{2/3}}{4\beta t}) \qquad (5.8)
\end{aligned}
$$

In the long time limit, $r >> r_0$ and $\beta t >> r$. Then (5.8) reduces to

$$< r^n >= \frac{1}{2}(\frac{4\beta t}{9})^{\frac{3n}{2}}\Gamma(\frac{3n+6}{2}) \qquad (5.9)$$

which is identical to what LaCasce (2010) showed. The asymptotic consideration above is valid since both the exponential and Kummer function go to one when the arguments go to zero[1](Abramowitz and Stegun, 1972).

First looking at the second order raw moment, the variance ($n = 2$), (5.8) yields

$$< r^2 >= \frac{1}{2}\Gamma(6)(\frac{4\beta t}{9})^3exp(-\frac{9r_0^{2/3}}{4\beta t})M(6,3,\frac{9r_0^{2/3}}{4\beta t}) \qquad (5.10)$$

while the asymptotic solution from (5.9) is simply

$$< r^2 >= 5.2675\beta^3t^3 \qquad (5.11)$$

Thus, the variance converges to the Richardson form (see Chapter 3.4.1) after sufficiently long time. So, the arguments of the Kummer Function and the exponential function determine how fast the dispersion in the energy cascading range reaches the cubic form. These arguments are dependent on the initial separation r_0 and time t.

The fourth order moment, the kurtosis, was given by (3.53) in Chapter 3.5. A substitution of (5.10) and (5.8) with $n = 4$ yields the full Richardson kurtosis.

[1] As they do since both are inversely proportional to time

$$
\begin{aligned}
Ku_r &= \frac{\frac{1}{2}\Gamma(9)\frac{4\beta t}{9})^6 exp(-\frac{9r_0^{2/3}}{4\beta t})M(9,3,\frac{9r_0^{2/3}}{4\beta t})}{\frac{1}{2}\Gamma(6)\frac{4\beta t}{9})^3 exp(-\frac{9r_0^{2/3}}{4\beta t})M(6,3,\frac{9r_0^{2/3}}{4\beta t})^2} \\
&= 2\frac{\Gamma(9)}{120^2}\frac{1}{exp(-\frac{9r_0^{2/3}}{4\beta t})}\frac{M(9,3,\frac{9r_0^{2/3}}{4\beta t})}{M(6,3,\frac{9r_0^{2/3}}{4\beta t})}
\end{aligned}
$$

In the asymptotic limit, the solution converges to

$$Ku_r = 2\frac{\Gamma(9)}{120^2} = 5.6 \tag{5.12}$$

which is consistent to LaCasce (2010). So, the full Richardson solution converges to a self similar probability function.

5.2 The basic assumptions

In Chapter 3, a number of *a priori* assumptions were shown to be fundamental in forming the theoretical framework used in this thesis. These assumptions are; two dimensionality, locality, isotropy, homogeneity and stationarity. The isotropic assumption is least obviously satisfied, but a test is easily done. Therefore, after a short discussion on the remaining assumptions, an extended discussion on the isotropic nature of the turbulence is given.

Homogeneous dispersion does not depend on location. Since the particles are initialized uniformly around a latitude, homogeneity is actually not explored in this thesis. It would have required targeted deployments over limited domains, as Huber et al. (2001) did. Generally, there are likely to be zonal differences in the Northern hemisphere due to the distinct Rossby wave pattern. Huber et al. (2001) detected no obvious meridional variations.

Stationarity is also hardly tested in this project. There are done runs for two months in different seasons and possible similarities will be the only sign. Since particles are deployed only once in each period, possible changes during that month are undeterminable. Huber et al. (2001) found no obvious seasonal differences in the extratropics.

Charney (1971) showed that turbulent motion in a QG flow has the same properties 2-D turbulence. In that sense, with the initial separations of 55.7km and 97.0km in mind, the turbulence considered here could be assumed to be 2-D. In addition, a test on the data set showed a mean vertical displacement between 0.5km and 3km after five days. The lowest values were at 12km at 60^o NS. The latter reflects the stably stratified stratosphere compared to the well mixed troposphere (Wallace and Hobbs, 2006). Thus, stratospheric dynamics are strongly 2-D.

5.2.1 The isotropic assumption

In many cases, the atmosphere does not obey the isotropic assumption implemented in 2-D turbulence theory. On large scales, the meridional variations of the Coriolis force and the temperature gradient provide a zonally anisotropic situation, illustrated by the westerlies in the extratropics. Thus, to discuss the results against the theory, a test on how close the data are to be perfectly isotropic, is needed. A sensitive way of doing this is to calculate the ratio between the root mean square (rms) separation in zonal and meridional direction.

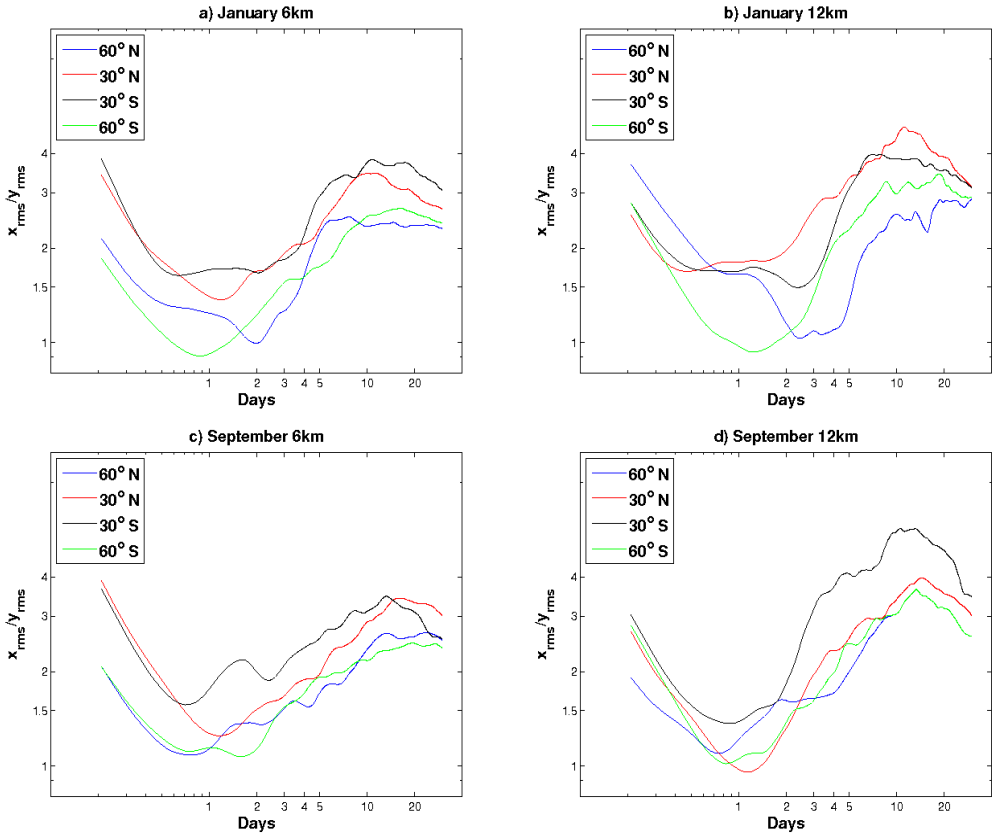

Figure 5.1: Zonal rms separation divided by meridional rms separation vs. time

The results are shown in Figure 5.1, where the ratio of x and y rms displacement is plotted versus time at four different latitudes at two altitudes in two months, i.e. all the data sets. The first hours are affected by the initial situation, as the separations are purely zonal. After that, a period of more or less constant ratios follows. Then the ratios increase, implying a transition from an isotropic to a zonally anisotropic range. The latter is associated with the intensifying zonal wind velocity component on large scales at these latitudes; subtropical and polar jet streams, dependent on latitude and season (Hartmann, 1994). The strong zonal shear accompanied with those winds will effectively separate the particles in the zonal direction. Thus, this range has to be considered by applying another theory on the zonal component; shear dispersion (Bennett, 1987). However, as pointed

out, this thesis is restricted to focus on the inertial range theory. Thus, the isotropic assumption has to be satisfied.

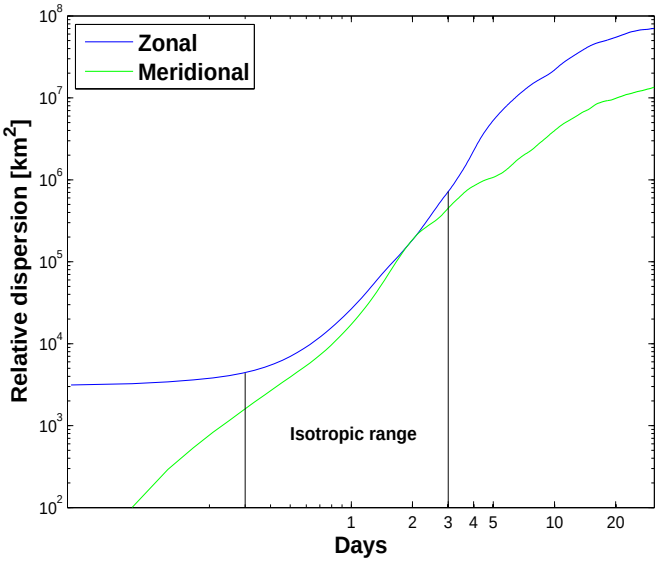

Figure 5.2: The two components of the relative dispersion at 60^{o}N at 6km in January 2009

First, the larger (zonal) initial separation at 30^o NS is illustrated at 6km by the generally higher ratios in the initial period here than at 60^o NS. Generally, the dynamics at the highest latitudes are more isotropic than the lowest ones. This could be reflected by a stronger jet stream with an associated stronger shear at those latitudes, i.e. the subtropical jet stream. Deviations from this are ratios at 30^0N in September, which indicate a fairly isotropic pattern. A weaker subtropical jet stream in the Northern hemispheric summer could probably explain that (Hartmann, 1994). There is also an earlier anisotropic tendency at 60^0N and 60^0S in September and January respectively. A relatively strong meridional component is more likely to appear in a winter hemisphere, because the meridional temperature gradient is stronger then. For this reason, isotropy can be maintained at larger scales in winter. These observations are not necessarily showing climatological characteristics, but specific weather patterns at these times.

Morel and Larcheveque (1974) did also test the isotropy in their data set. The rms ratio between the zonal and meridional component was remarkably close to unity from 100km to 1000km, but shifted to be heavily anisotropic beyond a scale of 1500km. Thus, the isotropic assumption is not unreasonable at the sub-deformation scale.

Generally, the ratios in Figure 5.1 agree exactly with what LaCasce (2010) found for the EOLE data. Thus, this is likely to be a general result. To a first approximation, the first three days could be assumed isotropic, suggested by Figure 5.2. By ruling out the differences observed in Figure 5.1 as

significant, a three days isotropic assumption applies in all cases. This limit is considered when the upcoming results are discussed.

5.3 Relative dispersion

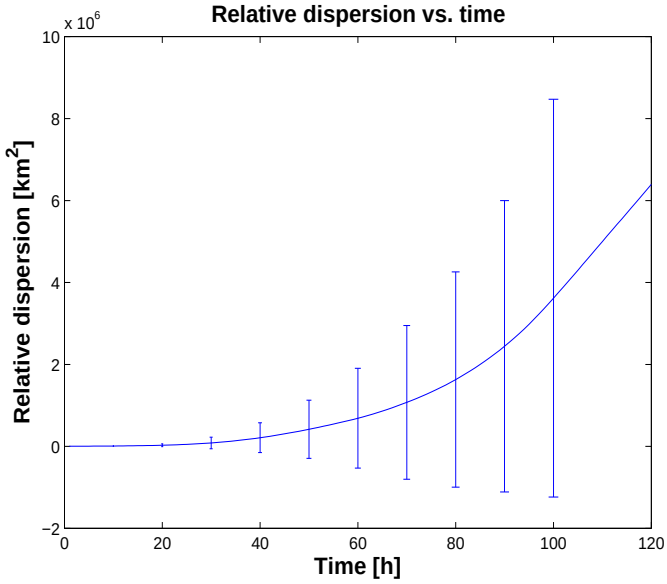

Figure 5.3: Relative dispersion vs. time for particles deployed at 6km along the latitude line 60^o N in January 2009. Each error bar displays one standard deviation

In this section, the results from the relative dispersion calculation will be presented. Figure 5.3 shows one relative dispersion test (6km at 60^oN in January 2009). The error bars indicate one standard deviation. This error measure is used instead of a standard error since all the data are shown to be highly non-Gaussian (see Section 5.5). However, the error bars are so large that zero separation cannot be ruled out, which is not very useful information. Thus, no error bars are plotted in the rest of this thesis.

In the rest of this section, several 60^o and 30^o data sets are shown. Linear regression on logarithmic and semilogarithmic plot is applied to fit power and exponential growth respectively. In accordance with 2-D turbulence theory, other power law findings than cubic are not shown (see Chapter 3.4). The initial separation for all the tests is the grid size, 1^o longitude (55.7km at 60^o NS and 96.4km at 30^o NS).

Figure 5.4 shows the relative dispersion at 6km at 60^o NS. During the first day, it grows exponentially up to separations of a few hundred kilometers. The e-folding time is about a third of a day. The initial separation of the fit is near the data initial separation. The further growth seems to obey a power law during the next two to three days. However, a fit is only displayed at 60^o N in January, since it provided a cubic growth, i.e. obeying the Richardson law. The remainings tend to either grow slightly slower or

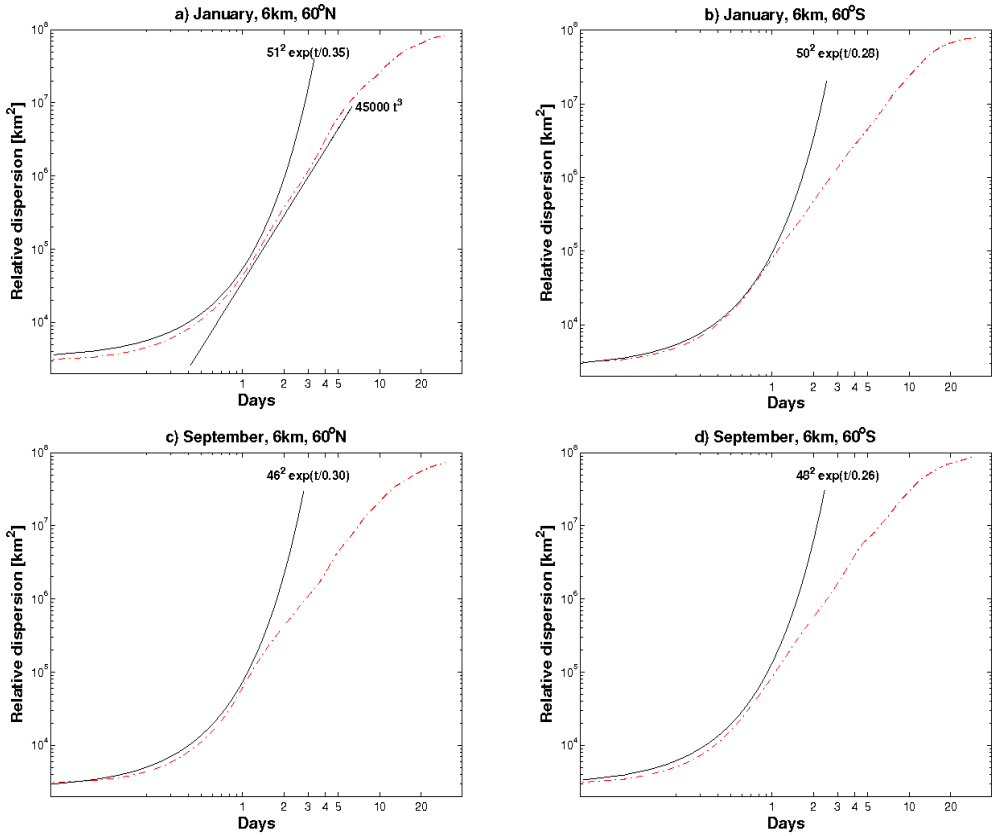

Figure 5.4: Relative dispersion vs. time for particles deployed at 6km along the latitude line 60^0 N (**a)** and **c)**) and 60^0 S (**b)** and **d)**) in January and September 2009

faster than cubic.

The relative dispersion at 12km is shown Figure 5.5. The results are quite similar to those at 6km, an exponential range lasting for approximately one day. However, the e-folding times are generally longer, about half a day, indicating slower exponential growths. The exception is at 60^0 N in September which yields the fastest e-folding times of all the tests in Figure 5.4 and 5.5.

The relative dispersion at 30^o N in September 2009 is shown in Figure 5.6. It does not seem to differ much compared to 60^o NS. The e-folding times are 0.45 at 6km and 0.35 at 12km.

According to Chapter 3.5.3, the corresponding diffusivity time scale T of the exponential range are eight times the e-folding time. Thus, for the high latitudes, the average time scale is $\sim$ 2.4 days at 6km and $\sim$ 3.8 days at 12km, if the very short time scale at 60^o N in September is ignored. The obvious deviations come solely from altitude differences. At 30^0N, the average diffusivity time scale is $\sim$ 3.3 and $\sim$ 3.1, respectively. An extended discussion on the altitude differences is available in Section 5.5.

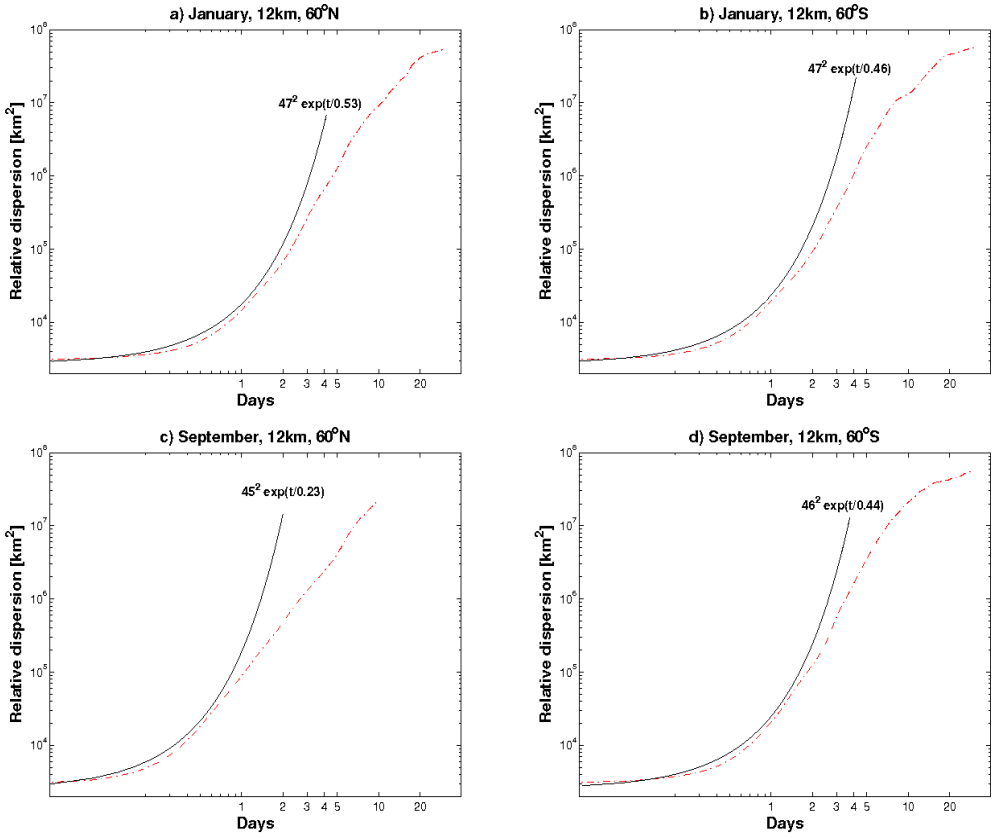

Figure 5.5: Relative dispersion vs. time for particles deployed at 12km along the latitude line 60^0 N (**a)** and **c)**) and 60^0 S (**b)** and **d)**) in January and September 2009

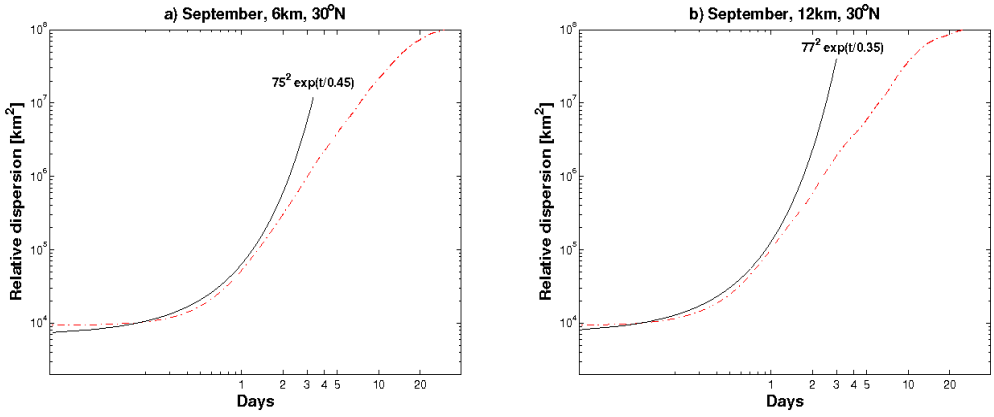

Figure 5.6: Relative dispersion vs. time for particles deployed along the latitude line 30^0 N in September 2009 at **a)** 6km and **b)** 12km

5.4 Kurtosis

In addition to the variance, higher order moments of the separation PDF can be applied to detect relative dispersion. The kurtosis, the fourth order raw moment given in (3.53) in Chapter 3.5 is a useful measure

to characterize the PDF. Since the Richardson distribution is self-similar, while the Lundgren distribution, indicating exponential growth, is not, the kurtosis can possibly distinguish between these two dispersion regimes. The time evolution of the zonal and meridional component of the relative displacement kurtosis is shown in Figure 5.7.

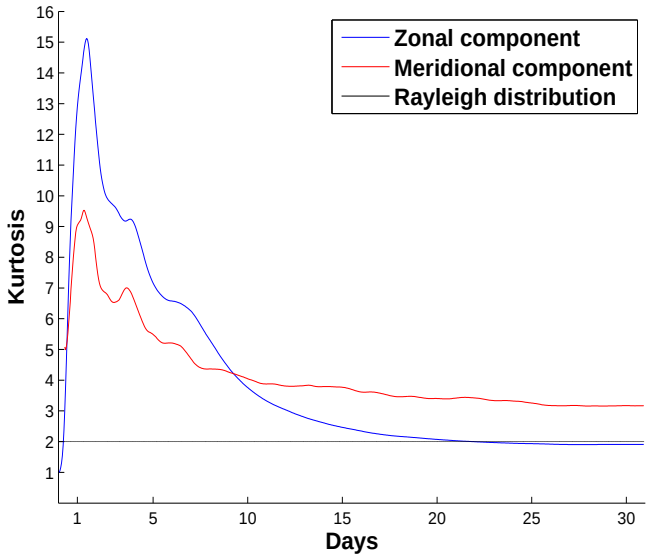

Figure 5.7: Kurtosis of the meridional relative displacement vs. time for particles deployed at 12km along the latitude line 30^o S in January 2009

The kurtosis provides a rather noisy behavior during the first days before it falls back to a constant value. The zonal component is close to two, i.e. a Rayleigh distribution, while the meridional component converges to a value between three and four. So the separation PDF is self-similar in the long-time limit, i.e. what to be expected with a diffusive process (see Chapter 3.5.4). An average of all the long-time values of the kurtosis yields 2.1 for the zonal component and 3.1 for the meridional.

According to the one day exponential fit of the relative dispersion detected in the previous chapter, an exponential growth of the kurtosis during the first 2-3 days is expected. (see Chapter 3.5.3). Thus, the early time blow up is likely to reflect that exponential range. However, this is heavily modified and the kurtosis becomes substantially smaller. Finally, it converges. When the full distribution includes separations experiencing dynamics at scales beyond the exponential range, its shape, i.e. the kurtosis, changes slightly because the separations at these large scales experience diffusive growth. In the end, the dispersion is purely diffusive, reflected by the constant kurtosis.

5.5 Probability density functions

As pointed out in Chapter 3.5, another tool to analyze relative dispersion is the probability density function (PDF) of the particle separations, of which relative dispersion is the second order moment. The relative dispersion and the kurtosis suggested an exponential range taken over by shear dispersion and finally a diffusive regime. By examining the whole distribution on the data sets, additional information about the dispersion are provided. While possible altitude differences were suggested by the relative dispersion, latitudinal dependence was rather hard to sort out. To obtain more information regarding these, all the PDFs are shown together. Then, the distributions are analyzed in light of 2-D theoretical predictions derived in Chapter 3.5. Finally, the renewed EOLE data set by LaCasce (2010) is compared with the most appropriate data set. All the figures show normalized PDFs, so the integral of the PDF function over separation is unity.

5.5.1 Comparison among the PDFs

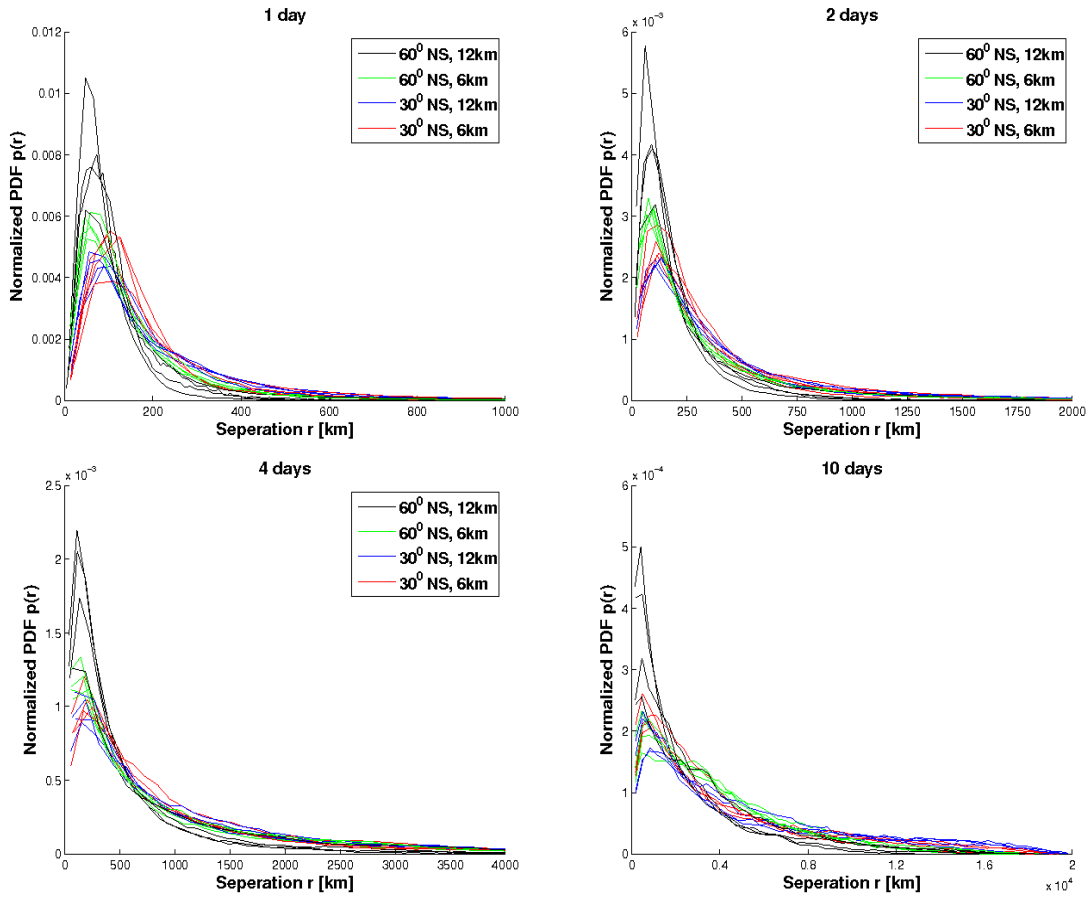

Figure 5.8: Normalized separation PDFs from all the data sets at four different times

Figure 5.8 shows the PDFs for all the data sets on four time steps, after 1 day, 2 days, 4 days and 10 days. An obvious difference is that with respect

to height at the high latitude. The distributions at 12km seem to be less spread out. This indicates a slower particle dispersion here than at 6km. At 30^o NS, the separation PDFs are slightly more spread out than at 60^o at 6km. After 10 days, the altitude difference at 60^o still remains.

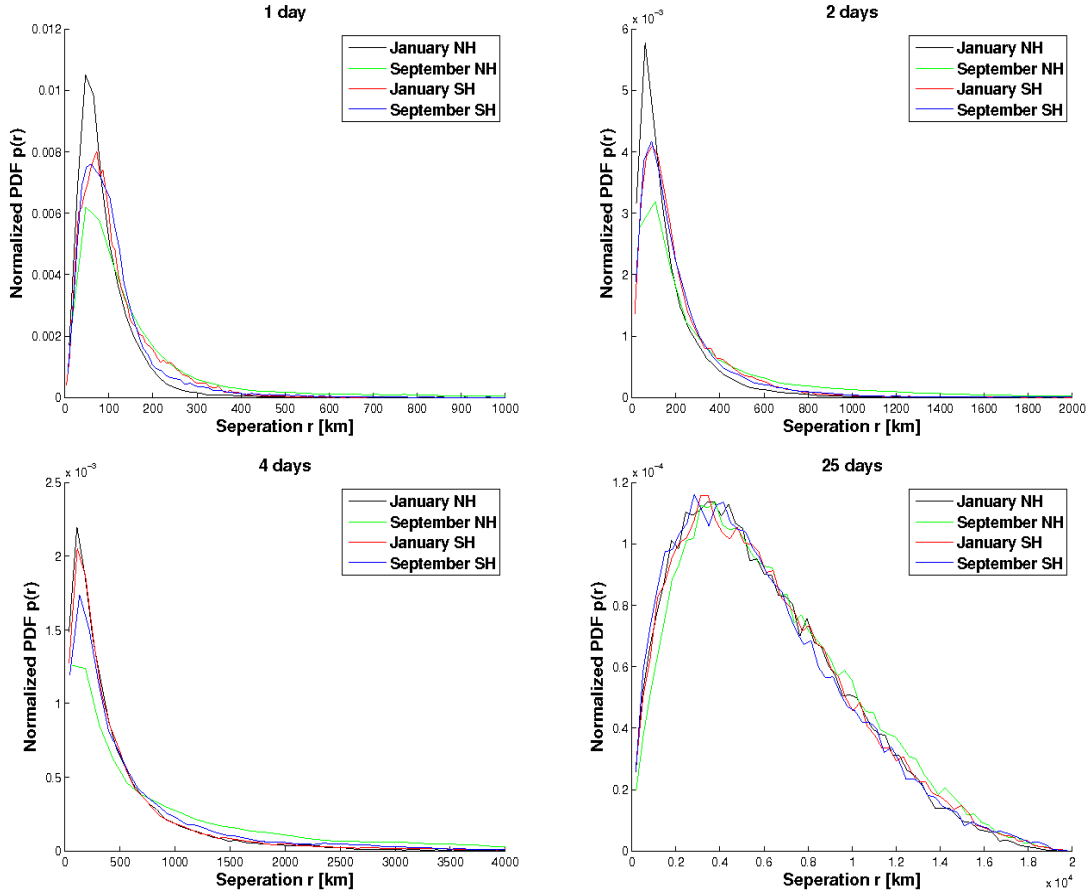

Figure 5.9: Normalized separation PDFs at 12km, 60^o NS at four different times

At 30^o NS, there is a tendency of larger amplitudes at 6km. However, the height differences are not that striking. There are no obvious differences among the distributions at 6km at 60^o NS. The details of the PDFs at 12km at 60^o NS are shown in Figure 5.9. While Southern hemisphere (SH) distributions are fairly similar the first two days, the Northern hemisphere (NH) distributions seem to behave differently. There is weaker dispersion in January than in September, reflected by the more spread out PDF in the latter. Actually, the separation distribution in September behaves quite similarly as the distributions at 6km (Figure 5.8). After four days, the SH distributions also deviate from each other. All data sets are distributed equally after 25 days. Thus, the large scale dispersion shows no seasonal dependence.

5.5.2 Comparison with theoretical functions

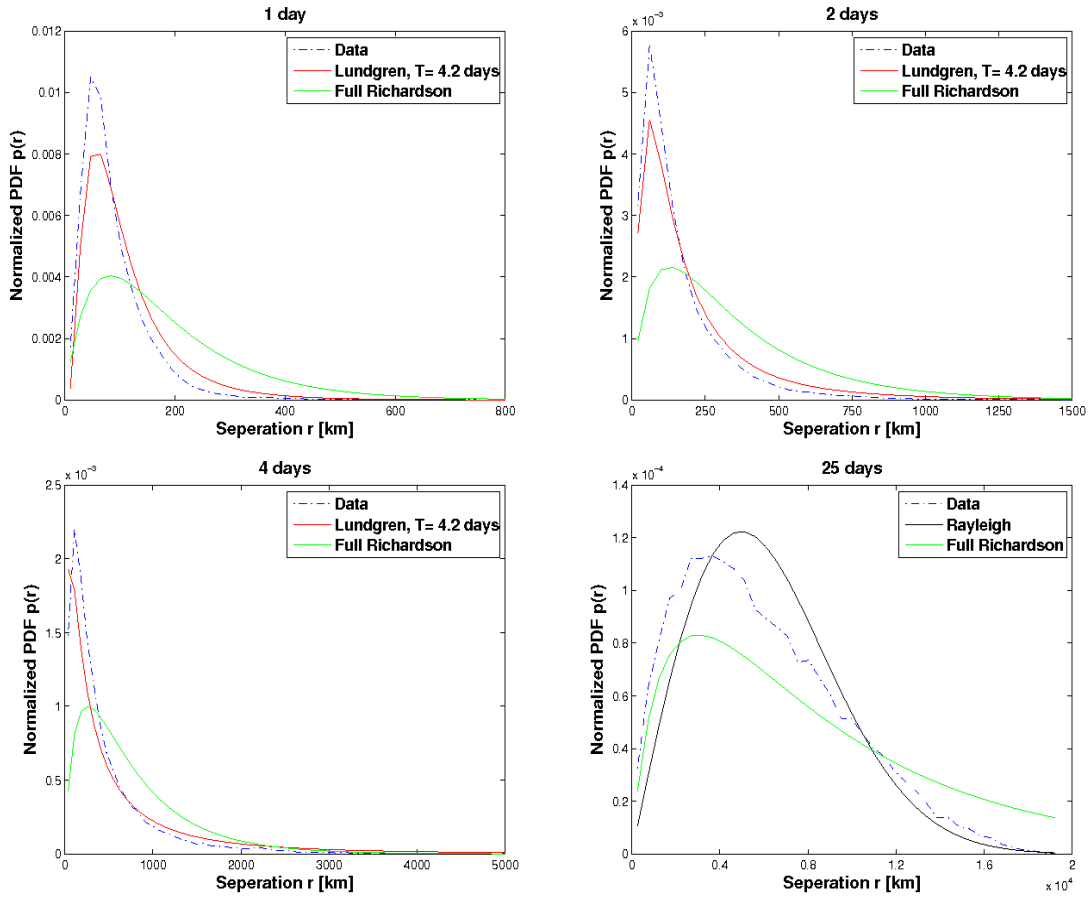

Figure 5.10: Normalized separation PDFs at 12km, 60^oN in January 2009 at four different times. The Lundgren function is calculated using $T = 4.2$ days. For the Richardson function, $\beta = 12.1km^{2/3}$/day. Both have the data initial separation, $r_0 = 55.7km$

In light of the considerations above, some of the separation distributions are plotted against the theoretical functions derived in Chapter 3.5, presented in Figure 5.10 - 5.12. The motivation is to possibly detect the relative dispersion growth characterizing the locations. The seasonal variations at 12km at 60^oN detected in the last subsection, will also be focused on.

The theoretical predictions are the Richardson, Lundgren and Rayleigh distributions from (3.51), (3.56) and (3.60) respectively, shown in Chapter 3.5. For the Richardson distribution, β was provided by fitting the Richardson variance (5.10), derived in Section 5.1, to the data dispersion. The diffusivity time scale T in the Lundgren distribution comes from the exponential fit of the relative dispersion in Section 5.3. Some figures include a comparison with an additional Lundgren distribution with a different T. This T is obtained by trying to fit the data PDF to a more appropriate Lundgren PDF. This method is only applied on PDFs which are far from being fitted by a Lundgren function with the T obtained via linear regression in Sec-

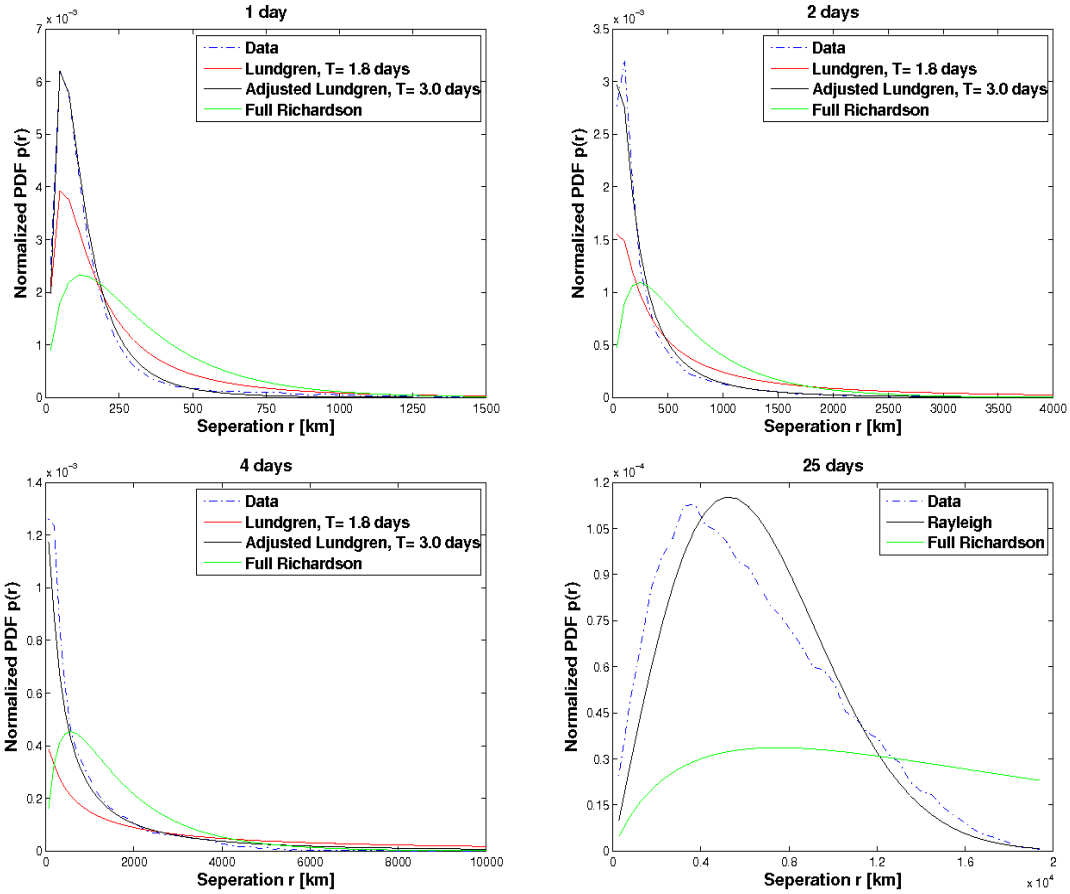

Figure 5.11: Normalized separation PDFs at 12km, 60^oN in September 2009 at four different times. The Lundgren functions are calculated using $T = 1.8$ days (the relative dispersion fit) and 3.0 days (the PDF fit). For the Richardson function, $\beta = 22.5\text{km}^{2/3}/\text{day}$. All have the data initial separation, $r_0 = 55.7\text{km}$

tion 5.3. All the diffusivity times, reflecting the exponential characteristics of the data, are listed in Table 5.5.2. For both the Lundgren and Richardson distribution, r_0 is the same as the data initial separation, i.e. the respective zonal grid size. For the Lundgren case, this is because the "effective" initial separation[2], shown in Figure 5.4- 5.6, is close to the data initial separation. The Rayleigh distribution is calculated using the variance of the data and is only shown in the long time limit. The Lundgren distribution is not shown after 25 days, since there are no expectations of exponential growth at that time (Chapter 3.4). Because of earlier observations of super-diffusive growth ($t^\alpha, \alpha > 1$) at large scales, e.g. (Ollitrault et al., 2005), the Richardson distribution is shown at this time as well.

Figure 5.10 shows the PDFs with the theoretical distributions in January 2009 at 60^0 N at 12km. The same location in September 2009 is shown in

[2]The "effective" initial separation is the initial separation associated with the relative dispersion fit

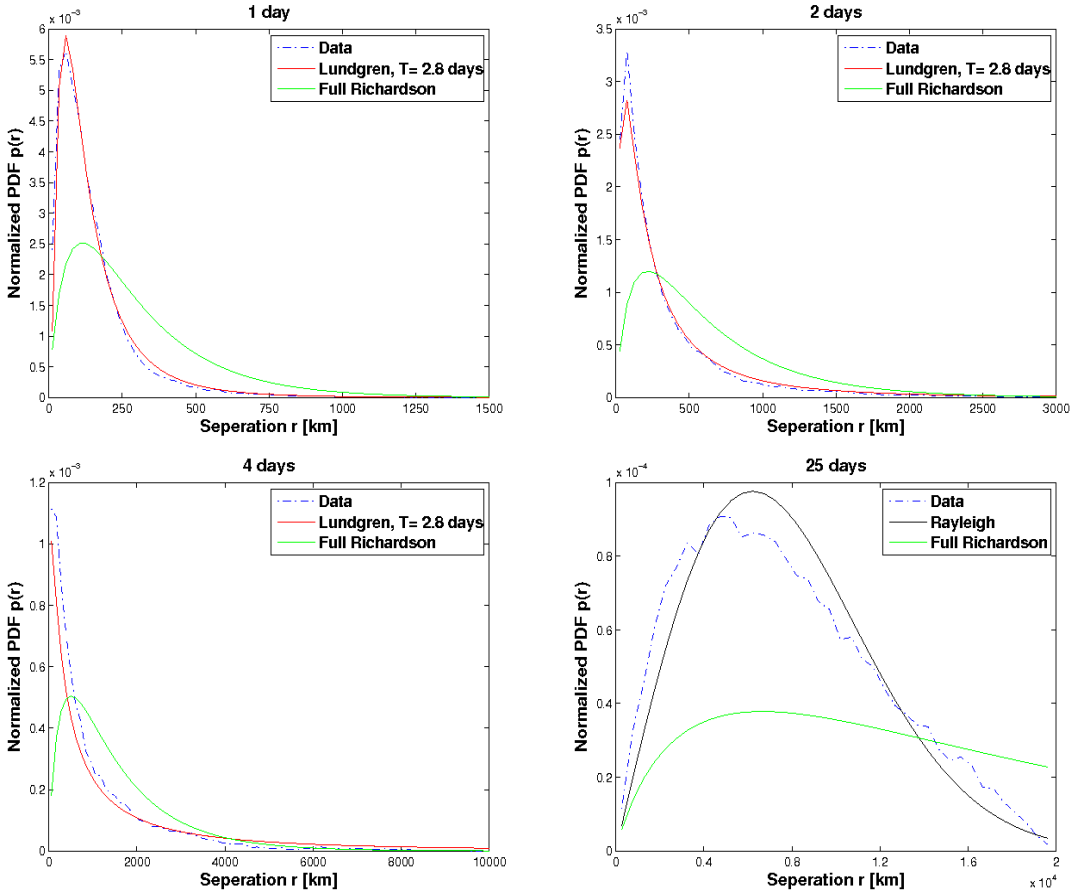

Figure 5.12: Normalized separation PDFs at 6km at 60^oN in January 2009 at four different times. The Lundgren function is calculated using $T = 2.8$ days. For the Richardson function, $\beta = 20.7km^{2/3}$/day. Both have the data initial separation, $r_0 = 55.7km$ distribution

Figure 5.11. It is obvious that both fit quite good to the Lundgren distribution with diffusivity times $T = 4.2$ and $T = 3.0$ respectively, though the latter had to be adjusted to fit (originally $T = 1.8$). Thus, the seasonal differences observed in Figure 5.9 are reflected by differences in the diffusivity time scales. The dispersion is exponential, but with faster growth in summer. The Lundgren function tends to exceed the data value at larger separation. This implies slower growth than exponential at the large scales, probably reflected by a diffusive regime here. A consequence is that the data PDF shows more rapid dispersion at the small scales. For SH, Table 5.5.2 shows equal time scales for both months.

In Figure 5.12, the PDF in NH January is shown to analyze the relative dispersion at 60^o at 6km. The data fit to the Lundgren function, which suggests exponential growth. Table 5.5.2 shows that the other data sets on the same latitude and height (60^o, 6km) provide more or less the same growth, suggesting negligible differences of the dispersion properties at this height. The adjusted growth rate at 12km in NH September is also more in line with those at 6km, supporting the observed similarities in Figure 5.8. The

Month	Height	60^o NH	30^o NH	30^o SH	60^o SH
January	6km	2.8	2.6	3.2	2.2
	12km	4.2	2.4	3.0	3.6
September	6km	2.4	3.6	3.7	**2.8**
	12km	**3.0**	**3.5**	3.3	3.6

Table 5.1: The diffusivity time scales for the best fit of the PDF to the Lundgren function. The bolded values are adjusted from the relative dispersion fit

PDFs at 30^oNS are not shown. The diffusivity times in Table 5.5.2 do support rather small dispersion differences at this latitude in line with Figure 5.8. The exception is in the NH winter, when the values are slightly lower.

After 25 days, the data fit quite well to the Rayleigh distribution. That is an indication of diffusive particle motions (see Chapter 3.5.4).

5.5.3 Comparison with a EOLE data set

The EOLE project was a pioneer in the 70's. A relatively large number of real balloons were launched in SH between August 1971 and July 1972 (see Chapter 4). Morel and Larcheveque (1974) examined the Lagrangian data to study atmospheric turbulent dispersion. The reexamination by LaCasce (2010) provided a renewed data set and calculated the separation distribution from these. Here follows a comparison between this EOLE data set and the model data from FLEXPART. This will also be a validation of the model data reliability.

The data set used here is that with "chance pairs" (see Chapter 4). This method provides more robust statistics (LaCasce, 2010) (see Chapter 4). The maximum initial separation is 25km, about the half of the model one at 60^o, i.e. 55.7km. In light of the location of this data set, i.e. at 200mb in SH, the model run at 60^o S at 12km in January 2009 was used for comparison.

The two data sets are shown in Figure 5.13. On the first three time steps, they fit properly. However, the EOLE data are noisier on the large separations. The PDF is also less spread out, reflected by a large amplitude somewhat shifted to the left after one day. This is probably due to the difference in initial separation and hence delayed EOLE balloons. The discrepancy is not present on the next time steps. The noise in the EOLE data is caused by the number of pairs, substantially lower than the 40000 provided by FLEXPART. This causes unstable statistics. After 25 days, the EOLE data distribution is too noisy to compare with the FLEXPART data. Generally, the results denote FLEXPART as a numerical model representing the mesocale processes impressively well.

5.6 Energy spectrum and structure function

As shown in Chapter 3.4, the Eulerian kinetic energy spectrum is related to the relative dispersion in 2-D turbulence theory. The underlying turbulence

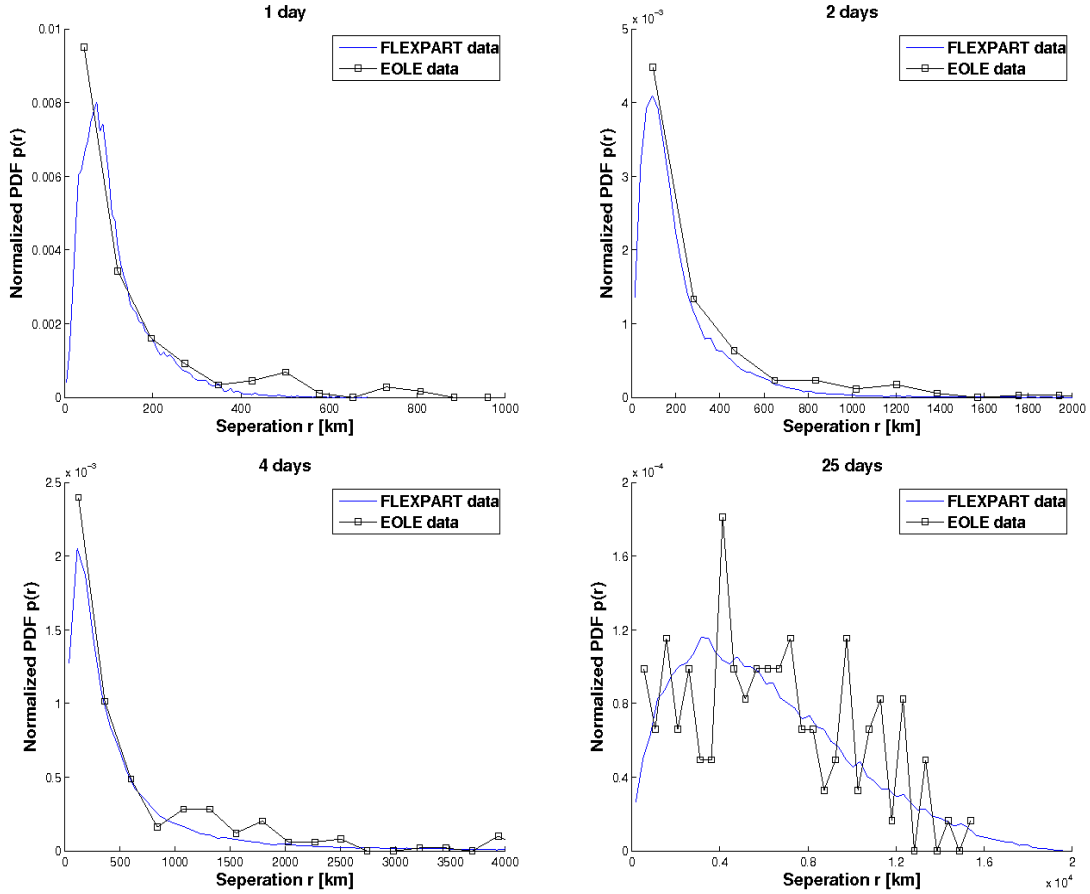

Figure 5.13: Normalized separation PDFs from the model data set (FLEXPART) and a balloon data set (EOLE). The model data are launched at 12km along the latitude line 60^oS in January 2009 with an initial separation, $r_0 = 55.7$. The balloon data are from the extratropics of Southern hemisphere with a maximum initial separation of 25km

determines how tracer particles are spread in the inertial range. Thus, the kinetic energy spectrum provides an additional tool to analyze the results presented in the previous sections. The velocity data used in this calculation are the model input wind field provided by ECMWF. These are horizontally evaluated on spherical coordinates and on pressure surfaces in the vertical (see Chapter 2). A data series around one single latitude circle throughout a month is used. The highest resolution provided is $0.2^o \times 0.2^o$, which is used here[3]. However, the kinetic energy spectrum with $1^o \times 1^o$ resolution is also shown. The spectra are calculated by applying the *pwelch method* on the velocity field (see Chapter 2.4).

Figure 5.14- 5.15 show the kinetic energy spectrum at 60^o S at 500hPa in January 2009. Up to wavelengths of $\simeq$ 2500km, the spectrum exhibits a k^{-3} dependence, indicating an enstrophy cascading range, i.e. nonlocal turbulence (see Chapter 3.2). The marked limit indicates a radius, i.e. one fourth

[3]The model run calculations are done on a $1^o \times 1^o$ horizontal grid (Chapter 2). Technical issues prevented a higher resolution in the model

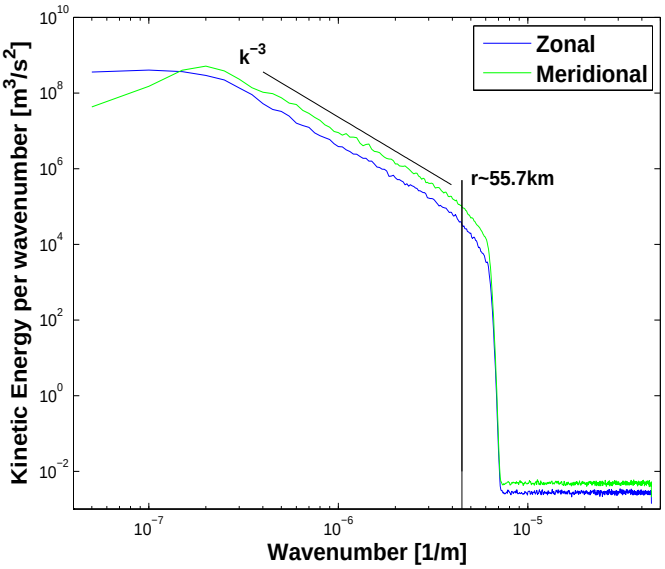

Figure 5.14: Eulerian kinetic energy spectrum at 500hPa, 60^0S in January 2009. The vertical line suggests the grid scale of the FLEXPART model, while the k^{-3} line indicate an enstrophy range. The horizontal resolution of the wind field is $0.2^o \times 0.2^o$

of a wavelength, which corresponds to the grid scale of the velocity field used in the model, $r \simeq 55.7$km. Around this scale, the spectral density suddenly falls down to smaller values. This could illustrate the limit of which scale the wind field is able to separate particles realistically, if a eddy radius is a typical relative dispersion scale. Then, Figure 5.15 is more relevant since it shows the spectrum with the same wind field resolution as used in the model. Below the grid scale, smaller separations would have been dispersed by a subgrid model parameterization added by a dissipated wind field. However, that should not cause problems for the results in this study since the initial separation is similar to the size of the grid scale. The relatively wider range of a dissipated spectrum in Figure 5.14 is unclear.

An alternate way of looking at the spectral behavior is with the second-order structure function (Lindborg, 1999). This was shown to be related to the energy spectrum under the homogeneous assumption Chapter 3.4. An advantage by using the structure function instead of the spectrum is the direct connection between scales. The pair separations in the relative dispersion are the same as the separation between the velocities in the structure function. The autocorrelation of the relative velocities, used to define the relative diffusivity in (3.25), is also related to the second-order structure function in a homogenous flow. This illustrates the connection to relative dispersion.

Figure 5.16 and 5.17 show the structure functions at some locations, picked out on the basis of the results in the previous sections. Generally, the motivation is to possibly explain the universal exponential growth, which

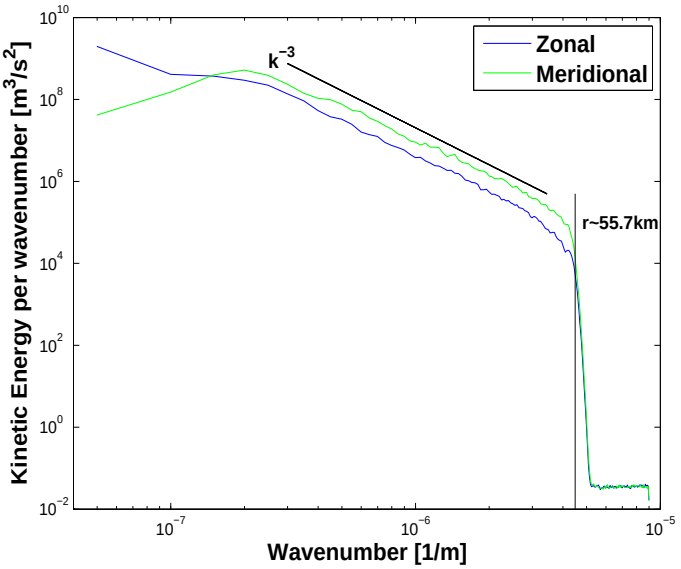

Figure 5.15: Eulerian kinetic energy spectrum at 500hPa, $60^0 S$ in January 2009. The vertical line suggests the grid scale of the FLEXPART model, while the k^{-3} line indicate an enstrophy range. The horizontal resolution of the wind field is $1^o \times 1^o$

was detected. The seasonal difference observed at 12km at 60^oN also needs to be clarified.

The second-order structure function at 60^o at 200hPa in NH is shown in Figure 5.16a) and b). Up to a few hundred kilometers, these suggest a r^2 dependence, which implies a kinetic energy spectrum with a k^{-3} slope, i.e. an enstrophy cascading range (see Chapter 3). Beyond that scale, the slope decays and flatten out towards the energy containing scale at about 2000km.

There are no obvious differences between the structure functions in Figure 5.16a) and b). To show possible differences due to altitude at 60^oN, the structure function at 500hPa in January is shown in Figure 5.16c). This yields more or less the same behavior as in a) and b). However, the r^2-range at 500hPa tends to flattens out sharper, while it extends to somewhat larger scales at 200hPa.

Figure 5.17 shows the second-order structure function at 30^oN in January. These also provide a r^2-range at the smallest scales. Both is quite similar to Figure 5.16c), according to the somewhat smaller scale the spectrum starts to level off.

Figure 5.18 shows a comparison among the structure functions with height at 60^oNS. The amplitudes at 500hPa are generally higher than at 200hPa.

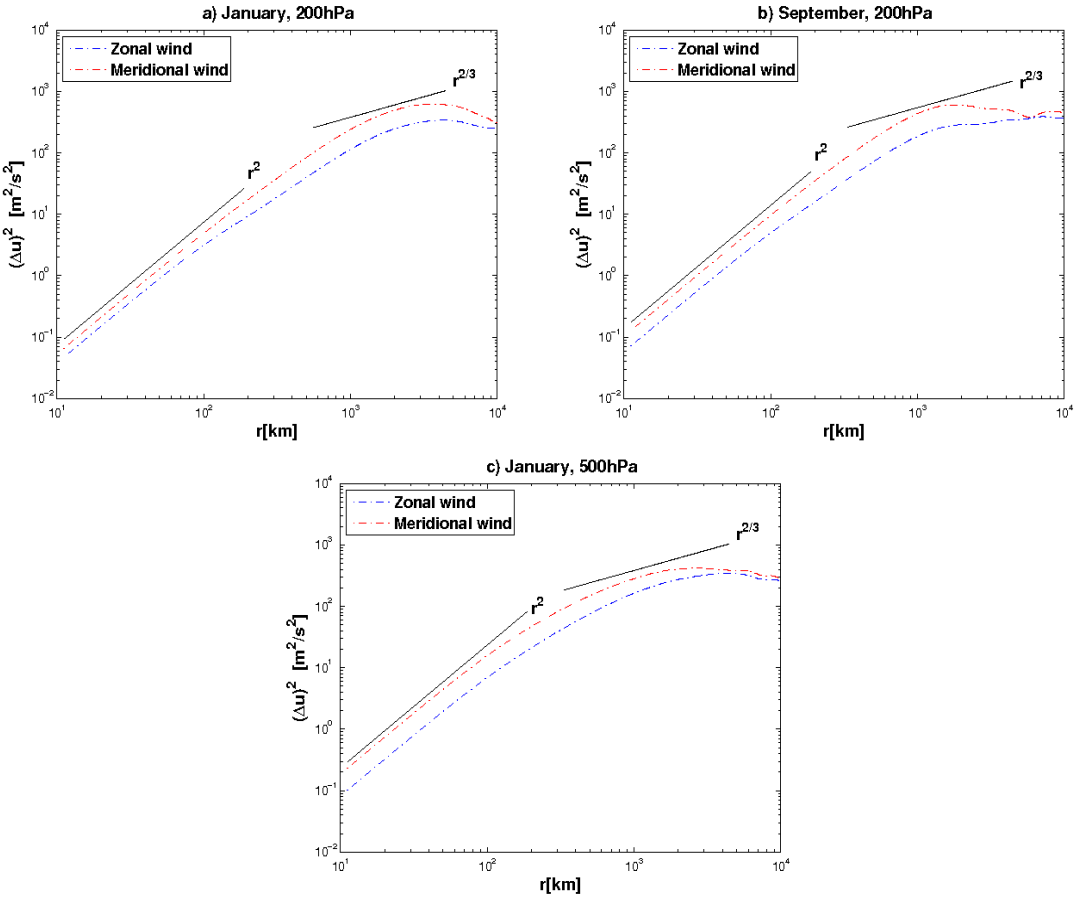

Figure 5.16: Second-order (Eulerian) structure functions at 200hPa (**a)** January 2009 and **b)** September 2009) and 500hPa (**c)** January 2009), 60^oN. The lines for the energy and enstrophy ranges are shown

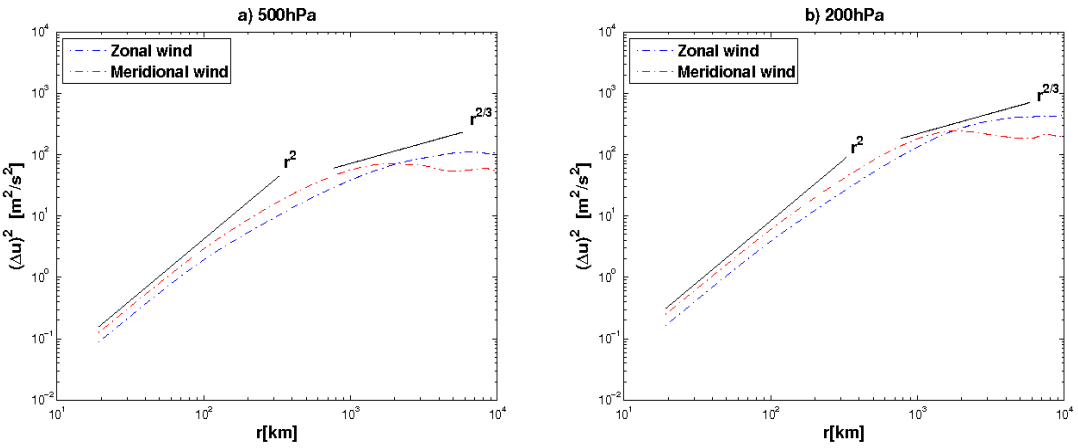

Figure 5.17: Second-order (Eulerian) structure functions at 500hPa (**a**) and 200hPa, (**b**), 30^0N, in January 2009. The lines for the energy and enstrophy ranges are shown

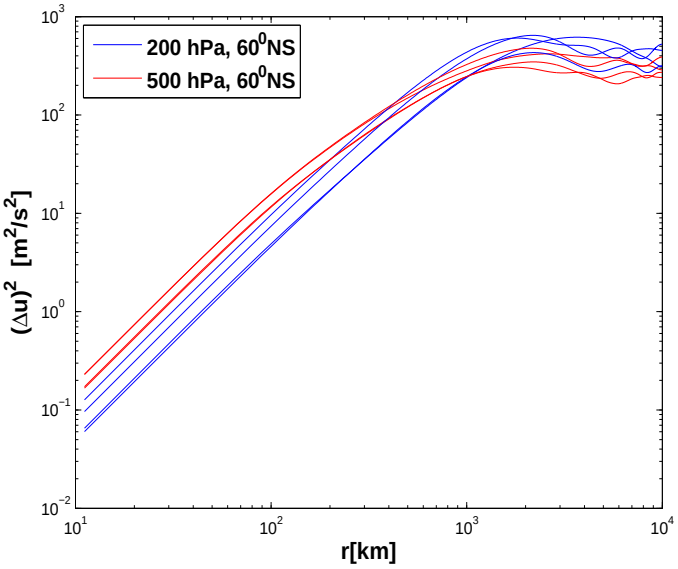

Figure 5.18: The meridional comoponent of the second-order (Eulerian) structure functions at 200hPa and 500hPa, 60^0NS in January and September 2009

Chapter 6

Discussion

In this chapter, the results based on the FLEXPART model runs presented in the Chapter 5 will be discussed and interpreted in light of each other. All the figures and tables which are referred to here are available in that chapter. Finally comes a short discussion of possible sources to errors and uncertainties.

6.1 Relative dispersion

The relative dispersion suggested exponential growth the first 1-2 days, taken over by a power law growth (Figure 5.4-5.6). As Figure 5.3 shows, any curve would eventually fit within the errors of the data after only a few days. Since the data are non-Gaussian, the variance is not able to describe how the relative dispersion behaves at each scale, i.e. it does not reflect the separation distribution alone. Therefore, relative dispersion is not very conclusive. Because isotropy is only reasonable to assume the first three days, an exponential growth is the only regime that can be inferred within this time period. The power law growth detected could possibly be a sign of shear dispersion (Bennett, 1987) as well as larger scale diffusive processes.

Generally, the e-folding times, given by the exponential argument in all the figures, suggest slower exponential dispersion growth at 12km than at 6km at 60^oNS. A discussion on possible reasons is given in the section covering the PDFs. At 30^o, there are no obvious differences in the exponential regime.

Viewed in light of other studies, the results of Morel and Larcheveque (1974) and Er-El and Peskin (1981) support the exponential growth detected here. The EOLE data set showed exponential growth up to 1000km with an e-folding time of 1.35 days, much larger than the values detected here. However, their fit is retrieved by fitting the data over a much longer period of time. The diffusivity times scales are in better accordance with the renewed EOLE data set by LaCasce (2010). This examination provided a three days exponential fit, in which the diffusivity time scale T was four days, generally in line with the data sets at 12km at 60^oNS. The EOLE balloons floated close to the tropopause, which is not unreasonable to assume

with the particles in this data set. A more complementary comparison with this data set was given in Section 5.5.3 and showed remarkable similarities. Lacorata et al. (2004) found an e-folding time of 0.5 days, however in an exponential regime just extending to 100km, by applying the method of FSLE (see Chapter 4). Huber et al. (2001) detected an average e-folding time of 3.6 days, but that was limited to the tropical region.

Huber et al. (2001) concluded that the extratropics are characterized by local dispersion in the inertial range, mainly ballistic growth, i.e. time squared. However, their results rely on an assumption of a 10 days fit, far from what is done here. The cubic growth detected in Figure 5.4a) is consistent with Lacorata et al. (2004), which suggested a Richardson regime beyond $\sim$ 100km by using the FSLE method on the EOLE data. Since this growth occurs on one single location, it is not very conclusive. Additionally, as pointed out above and even more important to note, the limited period of isotropy and the wide range of scales averaged in this method make the behavior after the exponential period hardly inferred. As emphasized in Chapter 3.5, relative dispersion is a limited descriptive tool to detect separation growth at certain scales. Higher order moments of the separation distribution, or the distribution itself, have to be considered to provide more information on how relative dispersion behaves.

6.2 Kurtosis

The exponential growth of relative dispersion is likely to be reflected by the kurtosis by the early time blow-up in Figure 5.7. It lasts for a few days in accordance with the relative dispersion exponential fit. The sudden stop and subsequent decaying period is possibly explained by a diffusive regime increasingly affecting the total dispersion. Finally, it converges to a constant value, which is reasonable to infer as a diffusive process. However, the zonal component value close to the Rayleigh raw kurtosis, i.e. 2, and the meridional somewhat higher are opposite to what being expected. A purely diffusive process for the meridional component and shear dispersion superimposed on diffusive growth for the zonal component is a more expected situation (Bennett, 1987).

The noisy initial behavior in Figure 5.7 was also captured by LaCasce and Bower (2000), though in the Atlantic Ocean. Er-El and Peskin (1981) also calculated the kurtosis for their subtropical release, but solely after five days, so the evolution is unknown. However, the value was 7.02 for the meridional component. This indicated, at least, a heavily non-Gaussian separation distribution and is in that sense consistent with the results here. Overall, the kurtosis provided no additional information of the relative dispersion in the inertial range. However, the behavior in the long time-limit is illustrated more clearly.

6.3 Probability density functions

As expected, the separation distributions in Figure 5.10-5.12 indicate the exponential growth suggested by the raw moments. However, due to the property of distinguishing separations, the PDFs confirm that a non-local regime is likely to extend beyond the time suggested by the moments. By analyzing relative dispersion, that could only be assumed since an energy injection scale at a few hundred kilometers is not expected in the atmosphere (see Chapter 3.2).

There were no clear height differences observed within the 30^o latitude range by Figure 5.8. That is also confirmed by Table 5.5.2. However, seasonal differences in the NH are reflected by a somewhat shorter diffusivity time in the winter. A strong subtropical jet stream present in this season (Hartmann, 1994) is likely to produce stronger mixing, reflected by faster growth rate here. At 60^oN, there are clearer indications of seasonal variations by Figure 5.9. However, more rapid dispersion in September at 12km than in January is unexpected, since the strong and meandering jet stream in the winter season is more likely to cause stronger mixing. These differences are not detected in SH at the same height. A possible explanation of these observations could be a seasonal variation of the tropopause height. At the latitude considered, there are likely to be more variations in the tropopause height in NH than in SH (Hoinka, 1998). If so, the distribution in September would reflect tropospheric dispersion, while that in January, as well as those at 60^oS would exhibit stratospheric dispersion. From Table 5.5.2, the diffusivity time scale in September NH is also quite similar to all values at 6km at 60^o, whose location definitely is below the tropopause. Thus, the seasonal variations shown could possibly be due to distinct dispersion regimes between the troposphere and the stratosphere. However, the tropopause height and its seasonal variations need to be more clarified. Since the dispersion is tested by only one time series during each season, the differences could be random and not a general property.

As pointed out in Section 5.5.2, some of the diffusivity time scales obtained from the relative dispersion fit had to be adjusted to fit more properly with the Lundgren distribution. At 12km at 60^oN in September, the value needed to be adjusted by more than a day. To possibly explain why that problem appears, both the relative dispersion fit and the adjusted PDF fit are shown together with this data set in Figure 6.1.

While the relative dispersion picks a longer time range fit (left side), starting slightly after a short initial period, the PDF fit belongs to that early period. In this case, the relative dispersion fit indicates more rapid dispersion than it really is, shown by the PDF in Figure 5.11. This error indicates that fitting the relative dispersion must be carefully done and might, in some cases, operate only as guidance to an appropriate fit to the Lundgren function. Generally, a test of slightly different fits than what obtained from the dispersion should be done in all studies like this.

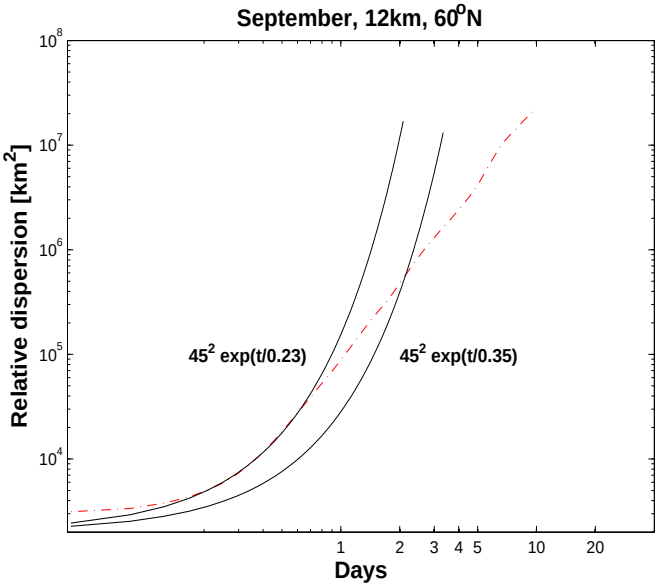

Figure 6.1: Relative dispersion vs. time for particles deployed uniformly around the latitude circle 60^{o}N at the altitude 12km in September 2009.

After 25 days, the data PDFs fit to the Rayleigh distribution. However, this prediction is also based on the isotropic assumption incorporated in 2-D turbulence theory (see Chapter 3.5.4). It is clear that the motion is far from isotropic at these scales. However, as remarked in the discussion of the kurtosis, it is likely that a diffusive process is characterizing both the zonal and meridional component, but with shear dispersion superimposed on the former (Bennett, 1987).

Summarized, the Richardson distribution does not fit properly at any time for any of the data sets. This suggests that the cubic growth Lacorata et al. (2004) inferred is hardly correct. It strengthens the results of Morel and Larcheveque (1974) and Er-El and Peskin (1981), which suggested exponential growth all over the mesoscale range up to 1000km. Er-El and Peskin (1981) found this regime at both high and low latitudes of the extratropics, which also supports the results here. Oceanic projects (LaCasce and Ohlmann, 2003; Ollitrault et al., 2005; Koszalka et al., 2009, e.g.) did also claim that sub-deformation relative dispersion growed exponentially. Huber et al. (2001) are in disagreement since exponential growth only was detected in the tropical region. However, the NH dispersion seemed to be a subject to seasonal changes, with enhanced stronger mixing in winter time. This thorough study also examined two different isentropic surfaces, but no obvious deviations were detected. It is also worth keeping in mind that the method Huber et al. (2001) use, contains some other properties and objectives. Especially the way dispersion is retrieved by a 10 days fit is substantially different. The use of 72 clusters spread over the whole sphere yields a study on zonal dependence in addition to the meridional. Since the particle clusters were deployed every 12 hour during the boreal summer and winter, Huber et al.

(2001) obtained more plausible seasonal and climatological characteristics.

6.4 The second-order structure function

Shown in Figure 5.16 and 5.17, a r^2-dependence of the second-order structure function was universal at the smallest scales. A reason for the gradual decrease of slope between the r^2-range and the energy injection scale is hardly suggested. However, the flattened shape around the energy input scale is probably a sign of diffusive behavior. Based on other studies, it is likely that the enstrophy range continues up to the deformation radius, where a transition to a diffusive field occurs. Gage and Nastrom (1986) suggested that the enstrophy range extended to wavelengths of $\simeq$ 2000km, i.e. $\simeq$ 500km scale for the particle separations. Also Cho and Lindborg (2001) detected an enstrophy cascade in the same range of scales. Thus, both are in line with the results here.

The observed r^2-dependence, indicating an enstrophy cascading inertial range, supports the universal exponential growth in the isotropic range lasting for the first three days (Chapter 3.4.2). There is no sign of a $r^{2/3}$-range, which would have suggested a local turbulence regime. Thus, with the PDF results in mind, it could surely be argued for nonlocal dispersion up to the deformation radius and hence that the Richardson dispersion inferred by Lacorata et al. (2004) can be ruled out.

The more extended r^2-range at 200mb than at 500mb is in line with Cho and Lindborg (2001), which observed an even cleaner r^2-range in the stratosphere than in the troposphere. The tropopause as a dynamical barrier will eventually create these two regimes. This is an interesting observation, since the PDFs, except of in September, inferred slower dispersion growth at 12km at 60^oNS than at other locations (Figure 5.8 and 5.9). By (3.44) in Section 3.4.2, the time scale is inversally proportional to the enstrophy dissipation rate. By applying the same dimensional arguments as for the energy spectrum in Section 3.2, the structure function is proportional to η. Thus, rapid growth rate, i.e. a short time scale, yields a larger amplitude of the structure function. By assuming that the structure functions actually exhibit an enstrophy range, this property is illustrated in Figure 5.18, where $500hPa$ is plotted against $200hPa$. Thus, the relatively slow relative dispersion growth at the high alitude at 60^oNS is reflected by a relatively small amplitude of the structure function.

6.5 Error and uncertainties

The model data and the advecting wind field from ECMWF include a complex system of various error and uncertainty sources. The interpretations of the results against the assumptions made in 2-D turbulence theory also need some attention. Here follows a short discussion on these issues.

As emphasized in Chapter 2, there are several potential error sources in the calculation of trajectories, some inherent in the model and other due to uncertainty in the advecting wind field. All numerical models cause errors growing in time, i.e. truncation errors. They arise from taking finite number of iteration steps in the trajectory calculation, which causes initial position errors to grow in time. Interpolation errors are made when the Eulerian input wind field is interpolated into the model temporal and spatial grid, i.e. instant the trajectory position. The velocity field itself is also subject to previous interpolation. Reanalysis data are a combination of model forecast and observational data interpolated on an Eulerian grid. Since the data are available only four times a day, pure forecast data are used at intermediate times to obtain a 3 hours temporal resolution. Forecast data are less reliable than reanalysis and hence increase the uncertainty.

As pointed out in the previous sections, the isotropic assumption is of fundamental importance when analyzing the dispersion against 2-D turbulence theory. Therefore, interpretations and statements have to be carefully done. In Section 5.1, it was shown that isotropy is a reasonable assumption during the first three days. Another important aspect with this study is the limited number of times, only two, at which dispersion has been tested. Therefore, suggestions and conclusions of particularly seasonal characteristics have to be carefully done. Additionally, there are uncertainties regarding the accordance between the heights and the pressure surfaces, were trajectories and the advecting field are evaluated, respectively. Hence, interpretations of altitudinal differences by using the second-order structure function are challenging.

Turbulence is described statistically and hence it needs to be analyzed with caution. Especially in the analysis of relative dispersion, any specific turbulence regime is hard to sort out. As observed in Section 5.3, the exponential growth was modified after fairly short time and no growth could be ruled out, also reflected by the large error bars in Figure 5.3. This complicates the choice of β and T, used for the theoretical separation distribution. Although the PDFs distinguish the separations, these are also affected by larger scales after only short time. Nevertheless, this measure gives a much more conclusive picture of the dispersion.

Chapter 7

Summary and conclusion

The main goal of this thesis was to study the characteristics of relative dispersion of passive tracers in the atmosphere. The Lagrangian transport model FLEXPART was used to generate particle trajectories. To detect possible variations due to season, height and geographical location, several runs were done; at four latitudes (60^0 and 30^0 in both hemispheres) at two heights (6km and 12km) during two months (January and September 2009). To study the dispersion, both relative dispersion itself and the probability density function of the separations were analyzed. These measures were presented in light of theoretical predictions, i.e. comparison with two turbulence scenarios; the Richardson´s cubic law and Lin's exponential law. The results were also compared with the data from the EOLE experiment examined by Morel and Larcheveque (1974). In addition, the reanalysis wind data, which advected the model "balloons", were used to calculate the second-order structure function. This yields a necessary interpretation tool to explain the dispersion behavior at each location.

Here follow some important concluding remarks of this thesis.

- Generally, the dispersion seems to be close to isotropic the first three days after launch. However, there are some variations due to location with generally more isotropic dispersion at the high latitudes. That the separations at 30^o are influenced by a stronger zonal wind field, i.e the subtropical jet stream, could explain these observations. The increasing anisotropic dispersion after three days put a limit on where the inertial range theory can be applied on the relative dispersion.

- The relative dispersion of the balloons grows exponentially during the first days. After that, it seems to obey a power law. Since the variance of the particle separations increases rapidly in time, relative dispersion becomes a time based average over a huge range of separations. Then the detected power law growth is hardly conclusive, any curve would equally well fit within the errors. The structure functions do neither show any conclusive at those scales. Thus, since the large scale dispersion is diffusive, indicated by the

kurtosis and the PDF in the long time limit, the intermediate range is likely to be an average of exponential growth at small scales and diffusive growth at large scales. Overall, relative dispersion is a limited measure in non-Gaussian distribution because of its lack of capability to reflect the distribution alone.

- Generally, the method using probability density functions of pair separations supports the exponential growth of the relative dispersion during the first days. The Lundgren PDF, which implies nonlocal dispersion, fits quite well to the data distribution, especially after short time. However, the tendency of the Lundgren distribution to exceed the data PDF at large separations shows the increasing diffusive influence from those scale with time. However, after four days, no other function than the Lundgren PDF is near to fit the data distribution. In the structure function, there were no signs of a Richardson regime beyond the small scale $r^2$2-range. Then, these results suggest that the power law growth inferred by Lacorata et al. (2004) and Huber et al. (2001) can be ruled out. As Morel and Larcheveque (1974) and Er-El and Peskin (1981) suggested, it is likely that the exponential range extends up to the radius of deformation and hence dispersion is suggested to be nonlocal.

- The diffusivity time scales suggest slower exponential growth rate at 12km than at 6km at 60^oNS. The exception is the dispersion at 12km in NH September, which is more in line with that at 6km. One possible explanation of these observations is a seasonal varying tropopause in NH, which caused the dispersion at 12km to be affected by tropospheric dynamics in summer and stratospheric dynamics in the winter. However, whether this behavior is random or general is unclear. The seasonal variations of the tropopause are also of high uncertainty. The time scales are in agreement with the studies of Lacorata et al. (2004) below 100km and LaCasce (2010), especially those at 12km at 60^oNS, except of that in September NH.

- A EOLE data set renewed by (LaCasce, 2010) was shown to be impressively equal to the separation distribution at 60^0S at 12km in January. In addition to support the nonlocal dispersion inferred by Morel and Larcheveque (1974), this comparison strengthens the reliability of the model data set. So, the dynamical processes at the mesoscale appear to be well described by FLEXPART.

- In light of the conclusions above, PDFs turn out to be a useful tool both to detect and interpret relative dispersion. In contrast to the separation variance, the full distribution makes it possible to distinguish the dispersion at different scales and hence describe a non-Gaussian PDF. Even under influence of shear dispersion and diffusive, it was possible to infer a specific dispersion regime.

- The structure functions calculated at 500hPa and 200hPa suggest a r^2-dependence below a scale of a few hundred kilometer. The shape of the kinetic energy spectrum is consequently k^{-3} , i.e. a weakly nonlocal enstrophy cascading inertial range. Generally, the structure functions calculated by Cho and Lindborg (2001) and the energy spectrum inferred by Nastrom and Gage (1984) support the observations here. However, the spectra are leveling off gradually towards the energy containing scale, of ambiguous reasons. The flattened shape at the large scales probably suggests a transition to a diffusive turbulence field. All these features support exponential dispersion taken over by diffusive dispersion at the energy containing scales, suggested by the PDFs. At 200mb, there is a tendency of an extended spatial range of the nonlocal cascade, which could be related to the slower exponential dispersion at 12km at 60^oNS. However, a more obvious correspondance is the somewhat smaller amplitudes of the structure functions corresponding to weaker relative dispersion.

The results of this thesis suggest that relative dispersion in the extratropics is nonlocal, both in the troposphere and the stratosphere. The reason for this is the observed enstrophy cascading range which dominates the mesoscale turbulent flow. The diffusivity time scales are longer at the highest altitude at 60^oNS, which could be explained by distinct dynamical differences across the tropopause. However, to be confirmed, more emphasis on stratospheric vs. tropospheric dispersion in future studies is needed. There are also other suggestions for future research on this topic. The tropical region, which were found to be characterized by exponential dispersion in that study, could be examined by a similar kind of model as FLEXPART. However, a problem might be the persistent convecting motion within the tropical region resulting in 3-D rather than 2-D turbulence. Also the mixing of particles in the storm tracks around 60^oN is an important issue. Differences likely to be along the latitude line are averaged out in this thesis. Thus, initializing particles at different spots could possibly explain more of the characteristics due to the trough-ridge pattern. Also an extended examination on temporal differences is needed. This study only considers two periods of time. Large scale dispersion is likely to be affected by long time trends and low frequent variability of the atmospheric dynamics. Wind field from a long period of years is available from ECMWF and could be used to possibly detect climatological variations.

The use of a numerical transport model, in this case FLEXPART, to study the dispersion characteristics in the 2-D turbulent atmosphere has proven to be beneficial. The large number of particles provided in such an experiment ensures stable statistics and more reliable results in that sense. The consistence with the EOLE balloon data set also suggests FLEXPART as a model that describes the physical processes at the mesoscale in a satisfactorily way. Thus, more use of numerical models could extend the understanding of 2-D turbulence. It is almost costless compared with big balloon projects.

Bibliography

Abramowitz, M and Stegun, I.A. (1972) Handbook of mathematical functions (Dover Publications).

Basdevant, C; Lesieur, M and Sadourny, R (1978) Subgrid-scale modeling of enstrophy transfer in two-dimensional turbulence. Journal of the Atmospheric Sciences, Vol. 35: p. 1028–1042.

Batchelor, G.K. (1953) The theory of homogenous turbulence. Camebridge University Press, Vol. 30: p. 9–13.

Bennett, A.F. (1984) Relative dispersion: local and nonlocal Dynamics. Journal of Atmospheric Sciences, Vol. 41: p. 1881–1886.

Bennett, A.F. (1987) A Lagrangian analysis of turbulent-diffusion. Reviews of Geophysics, Vol. 25(4): p. 799–822.

Bennett, A.F. (2006) Lagrangian Fluid Dynamics (Cambridge University Press).

Charney, J.G. (1971) Geostrophic turbulence. Journal of the Atmospheric Sciences, Vol. 28(6): p. 1087–&.

Cho, J.Y.N. and Lindborg, E (2001) Horizontal velocity structure functions in the upper troposphere and lower stratosphere 1. Observations. Journal of Geophysical Research-Atmospheres, Vol. 106(D10): p. 10 223–10 232.

Desbois, M (1975) Large-scale kinetic energy spectra from Eularian analysis of EOLE wind data. Journal of Atmospheric Sciences, Vol. 32: p. 1838–1847.

ECMWF (2002) IFS Documentation. ECMWF, available from *http//www.ecmwf.int*.

ECMWF (2011) The ERA-Interim reanalysis: Configuration and performance of the data assimilation system. ECMWF, ERA Report Series, available from *http//www.ecmwf.int*.

Er-El, J and Peskin, R.L (1981) Relative diffusion of constant-level balloons in the Southern hemisphere. Journal of Atmospheric Sciences, Vol. 38: p. 2264–2274.

Fjørtoft, R (1953) On the Changes in the Spectral Distribution of Kinetic Energy for Twodimensional, Nondivergent Flow. Tellus, Vol. 5(3).

Gage, K.S. and Nastrom, G.D. (1986) Theoretical interpretation of atmospheric wavenumber spectra wind and temperature observed by commercial aircraft during GASP. Journal of Atmospheric Sciences, Vol. 43: p. 729–740.

Gradshteyn, I.S. and Ryzhik, I.M. (1980) Table of integrals, series and products (Academic press).

Hartmann, D.L. (1994) Global Physical Climatology (Academic Press).

Hoinka, K.P. (1998) Statistics of the global tropopause pressure. Monthly Weather Review, Vol. 126(12): p. 3303–3325.

Holton, J.R. (2004) An introduction to dynamic meteorology, 4th edition (Elsevier Academic Press).

Huber, M; McWilliams, J.C. and Ghil, M (2001) A climatology of turbulent dispersion in the troposphere. American Meteorological Society, Vol. 58: p. 2377–2394.

Jullian, P; Massman, W and Levanon, N (1977) The TWERL Experiment:. Bulletin of the American Meteorological Society, Vol. 58: p. 936–948.

Kolmogorov, A.N. (1941) The local-structure of turbulence in incompressible viscous-fluid for very large reynolds-numbers. Doklady Akademii Nauk SSSR, Vol. 30: p. 9–13.

Koszalka, I.; LaCasce, J. H. and Orvik, K. A. (2009) Relative dispersion in the Nordic Seas. Journal of Marine Research, Vol. 67(4): p. 411–433.

Kraichnan, R.H. (1967) Inertial ranges in two-dimensional turbulence. Physics of Fluids, Vol. 10: p. 1417–1423.

LaCasce, J.H. (2008a) Lagrangian statistics from oceanic and atmospheric observations. Journal of Marine Research, Vol. 77: p. 1–29.

LaCasce, J.H. (2008b) Statistics from Lagrangian observations. Progress in Oceanography, Vol. 77: p. 1–29.

LaCasce, J.H. (2010) Relative displacement probability distribution functions from balloons and drifters. Journal of Marine Research, Vol. 68(3-4): p. 433–457.

LaCasce, J.H. (2011) Large Scale Turbulence in the Atmosphere and Ocean. Class notes, GEF4520, University of Oslo.

LaCasce, JH and Bower, A (2000) Relative dispersion in the subsurface North Atlantic. Journal of Marine Research, Vol. 58(6): p. 863–894.

LaCasce, J.H. and Ohlmann, C (2003) Relative dispersion at the surface of the Gulf of Mexico. Journal of Marine Research, Vol. 61(3): p. 285–312.

Lacorata, G; Aurell, E; Legras, B and Vulpiani, A (2004) Evidence for a k(-5/3) spectrum from the EOLE Lagrangian balloons in the low stratosphere. Journal of Atmospheric Sciences, Vol. 61: p. 2936–2942.

Lin, J (1972) Relative dispersion in enstrophy-cascading inertial range of homogeneous two-dimensional turbulence. Journal of the Atmospheric Sciences, Vol. 29: p. 394–&.

Lin, Y.L. (2007) Mesoscale dynamics (Cambridge University Press).

Lindborg, E (1999) Can the atmospheric kinetic energy spectrum be explained by two-dimensional turbulence?. Journal of Fluid Mechanics, Vol. 388: p. 259–288.

Lorenz, E.N. (1969) Predictability of a flow which posesses many scales of motion. Tellus, Vol. 21: p. 289–&.

Lundgren, T.S. (1981) Turbulent pair dispersion and scalar diffusion. Journal of Fluid Mechanics, Vol. 111: p. 27–57.

Maryon, R.H. (1998) Determining cross-wind variance for low frequency wind meander. Atmospheric Environment, Vol. 32(2): p. 115–121.

Morel, P and Bandeen, W (1973) Eole experiment - early results and current objectives. Bulletin of the American Meteorological Society, Vol. 54: p. 298–306.

Morel, P and Larcheveque, M (1974) Relative dispersion of constant-level balloons in the 200-mb general circulation. Journal of Atmospheric Sciences, Vol. 31: p. 2189–2196.

Nastrom, G.D. and Gage, K.S. (1984) A climatology of atmospheric wavenumber spectra of wind and temperature observed by commercial aircraft. Journal of Atmospheric Sciences, Vol. 42: p. 950–960.

Ollitrault, M; Gabillet, C and De Verdiere, AC (2005) Open ocean regimes of relative dispersion. Journal of Fluid Mechanics, Vol. 533: p. 381–407.

Papoulis, A (1991) Probability, Random Variables, and Stochastic Processes, 3rd edition (1cGraw-Hill).

Rhines, P.B. (1979) Geostrophic turbulence. Annual Review of Fluid Mechanics, Vol. 11: p. 401–441.

Richardson, L.F. (1926) Atmospheric diffusion shown on a distance-neighbour graph. Proceedings of the Royal Society of London, Series A, Vol. 110: p. 709–737.

Salmon, R (1980) Baroclinic instability and geostrophic turbulence. Geophysical and Astrophysical Fluid Dynamics, Vol. 15(3-4): p. 167–211.

Stohl, A; Forster, C; Frank, A; Seibert, P and Wotawa, G (2005) Technical note: The Lagrangian particle dispersion model FLEXPART 6.2. Atmospheric Chemistry and Physics, Vol. 2461-2474: p. 1881–1886.

Stohl, A and Seibert, P (1998) Accuracy of trajectories as determined from the conservation of meteorological tracers. Quarterly Journal of the Royal Meteorological Society, Vol. 124(549, Part A): p. 1465–1484.

Taylor, G.I. (1922) Diffusion by Continuous Movements. Proceedings of The London Mathematical Society, Vol. 20: p. 196–212.

Thomson, D.J. (1987) Criteria for the selection of stochastic-models of particle trajectories in turbulent flows. Journal of Fluid Mechanics, Vol. 180: p. 529–556.

Vallis, G. K. (2006) Atmospheric and Oceanic Fluid Dynamics (Cambridge University Press, Cambridge, U.K.).

Wallace, J.M. and Hobbs, P.V. (2006) Atmospheric science, An introduction survey, second edition (Elsvier Academic Press).

Welch, P.D. (1967) Use of fast Fourier transform for estimation of power spectra: A method based on time averaging over short modified periodograms. IEEE Transactions on Audio and Electroacoustics, Vol. AU15(2): p. 70–&.

Wilson, J.D. and Sawford, B.L. (1996) Review of Lagrangian stochastic models for trajectories in the turbulent atmosphere. Boundary-Layer Meteorology, Vol. 78(1-2): p. 191–210.